




Cite this: *RSC Adv.*, 2018, 8, 7651

# A short review of recent advances in CO<sub>2</sub> hydrogenation to hydrocarbons over heterogeneous catalysts

Wenhui Li,<sup>a</sup> Haozhi Wang,<sup>a</sup> Xiao Jiang,<sup>c</sup> Jie Zhu,<sup>a</sup> Zhongmin Liu,<sup>b</sup> Xinwen Guo <sup>\*a</sup> and Chunshan Song<sup>\*ac</sup>

CO<sub>2</sub> hydrogenation to hydrocarbons is a promising way of making waste to wealth and energy storage, which also solves the environmental and energy issues caused by CO<sub>2</sub> emissions. Much efforts and research are aimed at the conversion of CO<sub>2</sub> via hydrogenation to various value-added hydrocarbons, such as CH<sub>4</sub>, lower olefins, gasoline, or long-chain hydrocarbons catalyzed by different catalysts with various mechanisms. This review provides an overview of advances in CO<sub>2</sub> hydrogenation to hydrocarbons that have been achieved recently in terms of catalyst design, catalytic performance and reaction mechanism from both experiments and density functional theory calculations. In addition, the factors influencing the performance of catalysts and the first C–C coupling mechanism through different routes are also revealed. The fundamental factor for product selectivity is the surface H/C ratio adjusted by active metals, supports and promoters. Furthermore, the technical and application challenges of CO<sub>2</sub> conversion into useful fuels/chemicals are also summarized. To meet these challenges, future research directions are proposed in this review.

Received 21st December 2017  
 Accepted 30th January 2018

DOI: 10.1039/c7ra13546g

[rsc.li/rsc-advances](http://rsc.li/rsc-advances)

## 1. Introduction

Continuing consumption of fossil fuels worldwide has led to an increasing CO<sub>2</sub> concentration in the atmosphere, and global climate change caused by greenhouse gases has become a major challenge. Mitigation of CO<sub>2</sub> concentration in the atmosphere is in urgent need due to the continuing rise in atmospheric CO<sub>2</sub> concentration (*e.g.*, exceeding 400 ppm in 2016 (ref. 1)) and its negative and even possibly irreversible impact on the climate system. A recent report by UNEP (United Nations Environment Programme) estimated that if no firm global action is taken against climate change, temperatures might increase by more than 2 °C by 2050, and more than 4 °C by 2100.<sup>2</sup> In order to avoid this outcome, scientists indicate that global greenhouse gas emissions need to be reduced by at least 50% by 2050 compared to 1990, while the European Commission objective aims to achieve a reduction of 80–95% greenhouse gas emissions by 2050 compared to 1990.<sup>2</sup> A number of Europe's key

partners from all over the world, such as China, Brazil, and Korea, are addressing these issues through concrete actions to promote the “low carbon economy”.<sup>2</sup> The oil company TOTAL has generated its climate strategy based on the International Energy Agency's 2 °C scenario which aims to limit emissions to approximately 15 Gt CO<sub>2</sub>-eq. per year in 2050 with the objective to achieve carbon neutrality in the second half of the century.

At present, CO<sub>2</sub> can be reduced in three ways: control of CO<sub>2</sub> emissions, CO<sub>2</sub> capture and storage, and chemical conversion and utilization of CO<sub>2</sub>.<sup>3,4</sup> Carbon storage is important for cutting CO<sub>2</sub> emissions quickly, but has an issue of potential leakage of CO<sub>2</sub>.<sup>4,5</sup> CO<sub>2</sub> can be regarded as a carbon source to offer an alternative to produce carbon-containing value-added products and feedstocks. CO<sub>2</sub> obtained by capture not only can provide a pure carbon source for hydrogenation, but also can avoid the leakage problem caused by CO<sub>2</sub> storage. In addition, the National Aeronautics and Space Administration (NASA) also regarded the Sabatier reaction (CO<sub>2</sub> methanation) as a step in reclaiming oxygen within closed cycle life support systems.<sup>6,7</sup> Even the CO<sub>2</sub> in industrial flue gas can be used directly as a feed for hydrogenation.<sup>8</sup> Therefore, an efficient utilization of renewable carbon resources is crucial and beneficial to maintain a long-term and sustainable development of our society. CO<sub>2</sub> conversion requires energy input, and its conjunction with renewable energy would make this strategy more promising in terms of sustainability and environmental friendliness.

CO<sub>2</sub> reduction can be catalyzed through electrocatalysis,<sup>9</sup> photocatalysis,<sup>10</sup> and thermal catalysis. Among them, thermal

<sup>a</sup>State Key Laboratory of Fine Chemicals, PSU-DUT Joint Center for Energy Research, School of Chemical Engineering, Dalian University of Technology, Dalian 116024, P. R. China

<sup>b</sup>National Engineering Laboratory for Methanol to Olefins, Dalian National Laboratory for Clean Energy, Dalian Institute of Chemical Physics, Chinese Academy of Sciences, Dalian 116023, P. R. China

<sup>c</sup>Clean Fuels & Catalysis Program, EMS Energy Institute, PSU-DUT Joint Center for Energy Research, Departments of Energy and Mineral Engineering and Chemical Engineering, Pennsylvania State University, University Park, PA 16802, USA. E-mail: [guoxw@dlut.edu.cn](mailto:guoxw@dlut.edu.cn); [csong@psu.edu](mailto:csong@psu.edu)



catalysis receives significant attention due to its fast kinetics and flexible combination of active components. Carbon dioxide is a highly stable molecule, the activation and subsequent conversion of which alone are energy demanding. The addition of another substance with relatively higher Gibbs energy will make the  $\text{CO}_2$  conversion more favorable thermodynamically. However, electrocatalysis and photocatalysis have the fatal flaw of low energy efficiency. Therefore,  $\text{CO}_2$  hydrogenation<sup>11–14</sup> using  $\text{H}_2$  produced with renewable energy sources<sup>15,16</sup> is a promising research direction to produce chemicals and fuels,<sup>17–24</sup> which not only reduces the  $\text{CO}_2$  emissions, but also covers the shortage of fossil fuels.

Catalytic hydrogenation of  $\text{CO}_2$  using  $\text{H}_2$  produced with renewable energy is considered as a potential path forward for the sustainable production of lower olefins,<sup>25</sup> higher hydrocarbons,<sup>26</sup> formic acid,<sup>27</sup> methanol,<sup>28,29</sup> and higher alcohols<sup>30</sup> (Fig. 1). Considering the depletion of fossil fuels,  $\text{CO}_2$  hydrogenation to hydrocarbons is a promising way to convert  $\text{CO}_2$  into fuels among the other  $\text{CO}_2$  hydrogenation paths. Yet, we need to confront two challenges along with it: (1) sustainable hydrogen source and (2) dispersed product distribution. Much effort has been devoted to solving the former challenge, and scientists have already made great progress in water electrolysis to produce  $\text{H}_2$  using electricity generated with solar or wind or other renewable energy, and water splitting using photocatalytic, photoelectrochemical or other photochemical processes. There are established industrial technologies for water electrolysis with energy efficiencies of around 70%.<sup>31</sup> However, the  $\text{C}_{2+}$  hydrocarbons have a wide distribution. For example,  $\text{CH}_4$ ,  $\text{C}_2\text{--C}_4$ , and  $\text{C}_{5+}$  are targeted regions for production, while the selectivity was spread in a wide range, which becomes an obstruction to meet the requirement for real applications in industry. However, to date few reviews have dealt with the  $\text{CO}_2$  conversion mechanism and hydrocarbon chain growth both experimentally and with density functional theory (DFT) calculations. This review provides an overview of advances in  $\text{CO}_2$  hydrogenation to hydrocarbons that have been achieved recently in terms of catalyst design, catalytic performance and reaction mechanism from both experiments and DFT calculations. The review is organized based on some

apparent factors which affect catalyst performance and unified to the essential reason for  $\text{CO}_2$  hydrogenation that is the chemical state of the catalysts. The fundamental factor for product selectivity is the surface H/C ratio adjusted by the use of catalysts. In addition, DFT research advances are summarized from the point of view of C–O bond cleavage and C–C bond formation which gave a deep insight into  $\text{CO}_2$  activation and conversion. Guidance as to how to adjust the catalysts to promote hydrocarbon chain growth in  $\text{CO}_2$  conversion is also given in this review.

## 2. $\text{CO}_2$ hydrogenation to $\text{CH}_4$

$\text{CO}_2$  also can be identified as an energy carrier for the transformation of renewable energy. As aforementioned,  $\text{CO}_2$  hydrogenation to value-added products is one of the promising approaches to combat the  $\text{CO}_2$ -induced climate change, wherein the electrolysis of water to generate  $\text{H}_2$  with renewable energy is a potential energy storage approach, and would definitely add more credits to the establishment of such a sustainable carbon-based cycle. However, currently uses of renewable energy sources are limited by their inherent intermittency, and require scalable means of storage.<sup>32</sup> Therefore, the production of synthetic natural gas or liquid fuels is the most feasible and convenient way to store large amounts of intermittent energy produced from renewable sources for long periods. Among them, the so-called “power to gas” (PtG) concept has garnered significant attention (Fig. 2),<sup>33</sup> in which  $\text{CO}_2$  reacts with  $\text{H}_2$ , generated by water electrolysis with renewable wind or solar energy, to produce  $\text{CH}_4$  as an alternative source of natural gas. In Copenhagen, a commercial scale operation PtG project with 1.0 MW capacity was running successfully using transformation of the energy system toward a sustainable system in 2016.<sup>34</sup> From 2009 to 2013, there were five projects in Germany involving  $\text{CO}_2$  methanation at pilot plant or commercial scale with capacity ranging from 25 kW to 6300 kW.<sup>35</sup>

$\text{CO}_2$  methanation was first reported by the French chemist Paul Sabatier in 1902.<sup>36</sup> Due to the increasing demand for

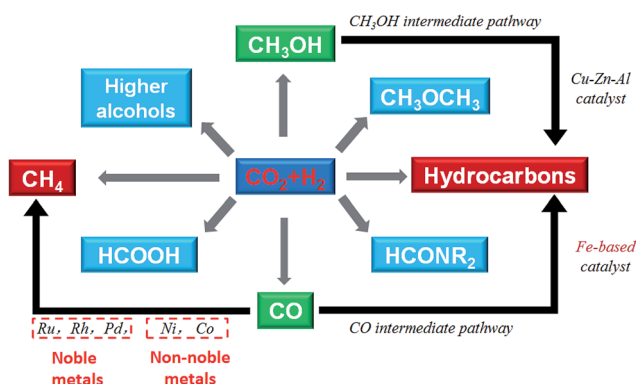


Fig. 1 Conversion of  $\text{CO}_2$  to chemicals and fuels through hydrogenation.

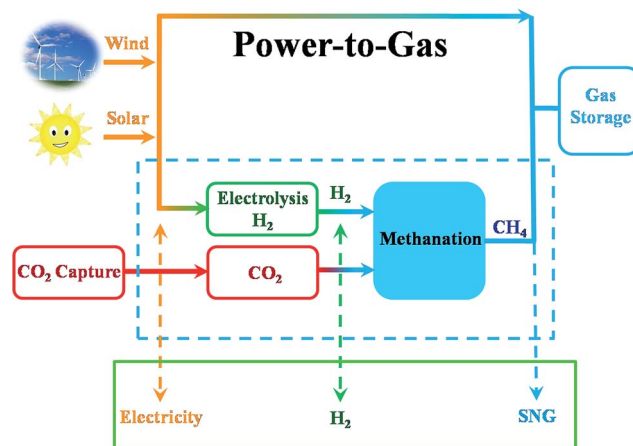


Fig. 2 Schematic illustration of  $\text{CO}_2$ -based sustainable production of chemicals and fuels.





Fig. 3 Equilibrium conversion of CO<sub>2</sub> in methanation at different temperatures (plotted using the data from the literature).<sup>39,40</sup>

mitigating global warming and storing surplus renewable power, this ancient art has attracted renewed attention. The Sabatier reaction is an advantageous way to store renewable energy such as wind and solar power, to transfer biogas effectively to biomethane, and to convert CO<sub>2</sub> to chemical feedstocks and fuels.<sup>37,38</sup> CO<sub>2</sub> methanation is exothermic with high equilibrium conversion between 25 °C and 400 °C as shown in Fig. 3.<sup>39,40</sup> CO<sub>2</sub> methanation can reach 99% CH<sub>4</sub> selectivity through use of appropriate catalysts, avoid the subsequent product separation and overcome the difficulty of dispersed product distribution. Therefore, such a thermodynamic feature makes CO<sub>2</sub> methanation more significant in terms of energy efficiency and economic viability.

## 2.1 Metal-based heterogeneous catalysts

CO<sub>2</sub> methanation can be catalyzed by transition metals such as Co,<sup>41–44</sup> Ni,<sup>7,45</sup> Ru,<sup>46,47</sup> Rh,<sup>48</sup> and Pd.<sup>49,50</sup> Based on previously published results, the activity performance of various metal-based catalysts decreases in the following order: Ru > Rh > Ni > Co > Pt > Pd.<sup>34</sup> Co- and Ni-based catalysts are preferred because of their low cost compared with the noble metals (Ru, Rh, Pd). Ni-based catalysts are the most commonly used for industrial purposes due to their high activity, high CH<sub>4</sub> selectivity, and easy availability. The catalytic performances of some representative catalysts are summarized in Table 1, as well as the preparation methods and reaction conditions.

**2.1.1 Metal-support interaction.** The traditional catalyst supports are the metal oxides Al<sub>2</sub>O<sub>3</sub>,<sup>21,51</sup> SiO<sub>2</sub>,<sup>52,53</sup> ZrO<sub>2</sub>,<sup>54</sup> TiO<sub>2</sub>,<sup>20,55</sup> and CeO<sub>2</sub> (ref. 19) and zeolites.<sup>7</sup> There are many factors concerning supports that can influence the performance of metal catalysts,<sup>56</sup> such as pore size,<sup>57</sup> structure of supports,<sup>42</sup> surface chemistry, and metal-support interaction.<sup>45,58–60</sup> Evidently, the activity and selectivity of these supported catalysts are sensitive to the interaction between the active metals and oxide supports.<sup>45,58–60</sup> Chen *et al.*<sup>61</sup> in a current perspective provide a bottom-up look at how the synergistic interactions at

the metal/oxide interface can tune the reaction mechanisms and in turn the selectivity of CO<sub>2</sub> hydrogenation. Actually, the metal sites on metal nanoparticles and the M<sup>+</sup> or O<sup>2-</sup> sites of oxides are observed to stabilize the key reaction intermediates, *e.g.*, \*CO<sub>2</sub>, \*C<sub>x</sub>H<sub>y</sub>, and \*C<sub>x</sub>H<sub>y</sub>O<sub>z</sub> species.

Zhou *et al.*<sup>63</sup> prepared a series of CeO<sub>2</sub>-supported Ni-based catalysts with various textural properties by hard-template method, soft-template method, and precipitation method, and examined their activity performance in CO<sub>2</sub> methanation. Among them, they found that the one prepared by the hard-template method exhibited a higher CO<sub>2</sub> methanation activity, and attributed such superiority to the mesoporous structure and high specific surface area. Furthermore, *in situ* FT-IR and *in situ* XPS results illustrate that the surface oxygen vacancies on the CeO<sub>2</sub> support were capable of activating the chemisorbed CO<sub>2</sub> and subsequently forming the CO intermediate.<sup>64</sup> Martin *et al.*<sup>65</sup> investigated Rh, Pd, and Ni catalysts supported on different substrates (Al<sub>2</sub>O<sub>3</sub>, CeO<sub>2</sub>, SiO<sub>2</sub>, and zeolites) for CO<sub>2</sub> methanation. Rh/Al<sub>2</sub>O<sub>3</sub> and Rh/CeO<sub>2</sub> exhibited the highest CO<sub>2</sub> conversion, but differed in mechanism. *In situ* DRIFTS interferograms showed that the linear Rh–CO species was evident on Rh/Al<sub>2</sub>O<sub>3</sub>, suggesting CO<sub>2</sub> dissociation, while the CO was formed through formate and carbonate intermediate species on Rh/CeO<sub>2</sub>. These advantageous results indicate that the surface oxygen vacancies on the CeO<sub>2</sub> substrate enabled the interaction with CO<sub>2</sub>, and promoted the CO<sub>2</sub> hydrogenation. Li *et al.*<sup>62</sup> prepared Co/ZrO<sub>2</sub> catalysts for CO<sub>2</sub> methanation, as well as Co/Al<sub>2</sub>O<sub>3</sub> catalysts for comparison. The Co/ZrO<sub>2</sub> catalysts displayed a higher CO<sub>2</sub> methanation activity with a practically stable performance even after 300 h on stream, while the Co/Al<sub>2</sub>O<sub>3</sub>, in contrast, deactivated rapidly within the same period of time. The Co–Zr interface was observed on the samples in reduced form, which enabled the redistribution of active Co on the ZrO<sub>2</sub> support due to the special metal–support interaction (Fig. 4). The special Co–Zr interface is crucial for the superior CO<sub>2</sub> methanation activity. Dreyer *et al.*<sup>66</sup> have investigated the influence of metal oxide support reducibility on Ru-based catalysts for CO<sub>2</sub> methanation. They pointed out that the intermediate CO should have an appropriate coverage and strong adsorption, which ensures the occurrence of H<sub>2</sub> dissociation. The reducible CeO<sub>2</sub> support is the most suitable to support Ru for CO<sub>2</sub> methanation compared with the irreducible Al<sub>2</sub>O<sub>3</sub> which gives a quasi-saturated CO adsorption and limits the co-adsorption of H<sub>2</sub> and reducible ZnO which has a weak CO adsorption and leads to the reverse water–gas shift (RWGS) reaction.

In addition, metal oxide supports with the same chemical composition and different crystal phase also have an influence on the chemical state of the supported metal. Kim *et al.*<sup>67</sup> synthesized monodispersed 2 nm RuO<sub>2</sub> nanoparticle colloidal suspension, and impregnated it onto TiO<sub>2</sub> with different crystal phases for CO<sub>2</sub> methanation. The activity and product selectivity were strongly dependent on the composition of different crystal phases of TiO<sub>2</sub>, wherein P25, with 20% of anatase and the rest of rutile, exhibited the highest CO<sub>2</sub> conversion and CH<sub>4</sub> selectivity. Inspired by these results, they further developed a fundamental understanding of the composition structure–



Table 1 Summary of various catalysts for CO<sub>2</sub> methanation

| Catalyst  | Preparation method                                 | Reactor                           | GHSV<br>[mL h <sup>-1</sup> g <sup>-1</sup> ] | <i>P</i><br>[MPa] | <i>T</i><br>[°C] | <i>X</i> <sub>CO<sub>2</sub></sub><br>[%] | <i>S</i> <sub>CH<sub>4</sub></sub><br>[%] | Stability tests                             | Ref. |
|---|--|-----------------------------------|---|-------------------|------------------|---|---|---|------|
| NiO–MgO@SiO <sub>2</sub>  | Co-precipitation method                            | Fixed-bed quartz reactor          | 90 000  | 0.1               | 300              | 80  | 97  | Stable after 100 h                          | 94   |
| NiWMgO <sub>x</sub>   | Precipitation                                      | Fix-bed quartz tube micro-reactor | 40 000  | 0.1               | 300              | 83  | 99  | Stable after 100 h                          | 74   |
| 15% Ni 2% La-hydroxalcite   | Co-precipitation method                            | Tubular quartz reactor            | 12 000  | —                 | 250              | 46.5                                      | 99  | Stable after 5 h                            | 75   |
| 10Ni/Ce–ZrO <sub>2</sub>  | Ammonia evaporation method                         | Fixed-bed quartz reactor          | 20 000  | —                 | 275              | 55  | 99.8                                      | Stable after 70 h                           | 88   |
| Ni/CeO <sub>2</sub>   | Excess impregnation                                | Fixed-bed quartz reactor          | 22 000  | 0.1               | 340              | 91.1                                      | 100                                       | Decreased by 18% after 700 min              | 64   |
| 14% Ni 7% Ce/USY  | Impregnation                                       | Flow tubular reactor in Pyrex     | 43 000  | 0.1               | 400              | 68.3                                      | 95.1                                      | Stable after 10 h                           | 95   |
| 10% Ni/MOF-5  | Impregnation                                       | Fixed-bed quartz reactor          | 2000  | 0.1               | 320              | 75.1                                      | 100                                       | Stable after 100 h                          | 84   |
| 20% Ni/55% γ-Al <sub>2</sub> O <sub>3</sub> –15% ZrO <sub>2</sub> –15% TiO <sub>2</sub> –15% CeO <sub>2</sub> | Impregnation                                       | Fix-bed quartz reactor            | 20 000  | 0.1               | 300              | 85  | 98  | Stable after 400 min                        | 79   |
| 80% Ni–Al hydroxalcite  | Co-precipitation method                            | Fix-bed quartz reactor            | 20 000  | 0.1               | 300              | 86  | 98  | Stable after 25 h                           | 80   |
| 2.5% Ce–10% Ni/Al <sub>2</sub> O <sub>3</sub>   | Ultrasonic impregnation                            | Fixed-bed reactor                 | 7200  | 0.1               | 400              | 74  | 98  | —   | 17   |
| 12% Ni/Al <sub>2</sub> O <sub>3</sub> (3DFD structure)  | Impregnation, coated on 3DFD structures            | Fix-bed quartz tubular reactor    | 1500  | 0.1               | 350              | 85  | 98  | Stable after 53 h                           | 90   |
| 10% Ni/TiO <sub>2</sub>   | Dielectric barrier discharge plasma                | Fix-bed quartz tubular reactor    | 60 000  | 0.1               | 350              | 73.2                                      | 99  | —   | 91   |
| RQ Ni   | Rapid quenching                                    | Capacity hastelloy autoclave      | —   | 3                 | 200              | 60  | 99  | Five successive cycles without reactivation | 78   |
| 10Ni3Pr/Al <sub>2</sub> O <sub>3</sub>  | Evaporation induced self-assembly                  | Fix-bed quartz tubular reactor    | 15 000  | 0.1               | 400              | 76  | 98  | Stable after 50 h                           | 76   |
| 0.03% Pt–20% Co–80% Al <sub>2</sub> O <sub>3</sub>  | Double flame spray pyrolysis                       | U-shaped tube reactor             | 36 000  | 0.1               | 400              | 70  | 98  | —   | 89   |
| Co/(0.01)PC-600   | ZIF-67-derived carbonization                       | Fix-bed reactor                   | 72 000  | 3                 | 270              | 59  | 99  | Stable after 420 min                        | 85   |
| Pt@CSN  | Water-soaking-assisted phase-transformation method | Fix-bed reactor                   | 4800  | 3                 | 320              | 41.8                                      | 95  | —   | 87   |
| 10Co/ZrO <sub>2</sub>   | Impregnation                                       | Fix-bed reactor                   | 3600  | 3                 | 400              | 92.5                                      | 99  | Stable after 300 h                          | 62   |
| 20% Co/KIT-6  | Impregnation                                       | Fix-bed quartz tubular reactor    | 22 000  | 0.1               | 260              | 46  | 99  | —   | 42   |
| 2.5% Ru/P25   | Impregnation                                       | Continuous flow fixed-bed reactor | 6000  | 0.1               | 200              | 27.4                                      | 100                                       | —   | 67   |
| Ru/CeO <sub>2</sub>   | Single-step flame spray pyrolysis                  | Fix-bed reactor                   | 7640  | —                 | 300              | 83  | 99  | —   | 66   |

activity performance relationship.<sup>68</sup> The phenomenon that RuO<sub>2</sub> nanoparticles tended to migrate towards rutile TiO<sub>2</sub> during the CO<sub>2</sub> methanation process when rutile and anatase TiO<sub>2</sub> co-existed was evidenced by the stabilization of RuO<sub>2</sub> on rutile TiO<sub>2</sub> based on characterization results. Such rutile-favored migration led to the formation of highly dispersed Ru in the reduced form, thereby exhibiting a superior activity (Fig. 5). Lin *et al.*<sup>69</sup> also observed a similar phenomenon on Ni/TiO<sub>2</sub> catalysts with different TiO<sub>2</sub> crystal phases for both CO and CO<sub>2</sub> methanation. Chen *et al.*<sup>56</sup> found that PtCo bimetallic catalysts were capable of shifting the selectivity from CO to CH<sub>4</sub> by altering the oxide supports from TiO<sub>2</sub> to ZrO<sub>2</sub>, respectively. In other words, PtCo/ZrO<sub>2</sub> tends to favor CH<sub>4</sub> formation compared with PtCo/TiO<sub>2</sub>. Both XPS and DFT calculations were carried out to elucidate the origins for CO formation on PtCo/TiO<sub>2</sub> and CH<sub>4</sub> formation on PtCo/ZrO<sub>2</sub>. Experimentally, both \*HCOO and \*HOCO were identified as reaction intermediates on both PtCo/

TiO<sub>2</sub> and PtCo/ZrO<sub>2</sub>, whereas \*CH<sub>3</sub>O was only evidenced on PtCo/ZrO<sub>2</sub>. DFT results illustrate that the CO desorption energy is much lower than that of its hydrogenation to \*CHO on PtCo/TiO<sub>2</sub>. Therefore, the chemisorbed CO favored desorption energetically rather than the subsequent hydrogenation, thereby leading to a selective production of CO. On the other hand, CO formation was hindered on PtCo/ZrO<sub>2</sub> catalyst, and CH<sub>4</sub> was formed. Apparently, the interaction between metal and support plays an important role in product selectivity.

**2.1.2 Effect of metal particle size.** In addition to metal-support interaction, the particle size also strongly affects the kinetic parameters of CO<sub>2</sub> hydrogenation. Wu *et al.* tested Ni/SiO<sub>2</sub> catalysts with different metal loadings, namely 0.5 wt% and 10 wt%, in CO<sub>2</sub> methanation, the loading levels of which corresponded to small Ni clusters and large Ni particles, respectively. CO formation was favored on the small Ni clusters, while more CH<sub>4</sub> was produced on the large Ni particles.<sup>70</sup> A





Fig. 4 STEM-EDS maps and corresponding TEM images of (a) calcined catalyst precursors  $\text{Co}_3\text{O}_4/\text{ZrO}_2$  and (b) reduced catalyst  $\text{Co}/\text{ZrO}_2$ . Reprinted with permission from ref. 62. Copyright 2017 Elsevier.

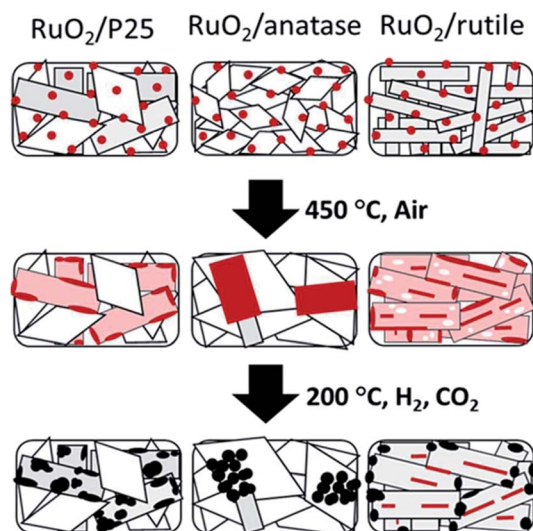


Fig. 5 Schematic illustration of the shape evolution of  $\text{RuO}_2/\text{TiO}_2$  catalysts: after  $\text{RuO}_2$  nanoparticle deposition, after thermal annealing at  $450\text{ }^\circ\text{C}$ , and after reduction and methanation. Red indicates  $\text{RuO}_2$ , pink indicates thin  $\text{RuO}_2$  layer, white indicates Ru depleted area, and black indicates metallic Ru. Reprinted with permission from ref. 67. Copyright 2013 RSC.

similar phenomenon was also evidenced on  $\text{Ru}/\text{Al}_2\text{O}_3$  catalysts by Kwak *et al.*,<sup>47</sup> wherein 1 wt%  $\text{Ru}/\text{Al}_2\text{O}_3$  with highly dispersed particles selectively produced CO, and the selectivity was gradually shifted to  $\text{CH}_4$  along with sintering degree of Ru nanoparticles with an increase of Ru loading levels. At 5% of Ru loading, the catalyst had large Ru clusters, therefore making the reaction proceed all the way to  $\text{CH}_4$  (Fig. 6). Iablokov *et al.*<sup>71</sup> investigated the influence of Co particle size on the activity and selectivity of  $\text{CO}_2$  methanation. A series of near-monodisperse Co nanoparticles with size in the range 3–10 nm were

prepared using oleic acid and  $\text{Co}_2(\text{CO})_8$ , among which the larger Co particles exhibited a higher turnover frequency (TOF). Christopher *et al.*<sup>72</sup> investigated the quantitative relationship between the concentrations of isolated  $\text{Rh}_{\text{iso}}$  active sites and Rh nanoparticles supported on  $\text{TiO}_2$  and the product distribution for  $\text{CO}_2$  thermal reduction. Evidently, the isolated Rh sites favored CO formation, and the  $\text{CH}_4$  selectivity increased with the decrease of  $\text{Rh}_{\text{iso}}$  fraction.

Seen from the results above, both noble and non-noble metal-based catalysts can be applied to  $\text{CO}_2$  methanation, and the experimental results indicate that, within a certain range of metal particle size, the atom-scale structured catalysts tend to favor the RWGS reaction, while the larger metal particles facilitate  $\text{CH}_4$  formation.<sup>50</sup> To unveil the underlying reasons behind the size-dependent effect, Ma *et al.*<sup>73</sup> prepared  $\text{Ir}/\text{CeO}_2$  catalysts with various Ir loadings using a ligand-free method, and tested them in  $\text{CO}_2$  methanation. The catalysts with low Ir loading presented partially oxidized Ir species, and displayed catalytic selectivity for CO production. On the other hand, more metallic Ir species appeared to emerge when increasing the Ir loading level, leading to a preference for desired  $\text{CH}_4$  formation. Their results suggest that the chemical state of Ir could be finely tuned by altering the loading of the metal. Actually, the particle size effect is the chemical state effect. The metal loading essentially affects the active metal state on the supports and further affects the reaction routes.

**2.1.3 Multi-component metal catalysts.** The surface properties are also a significant factor in addition to the metal-support interaction and particle size effect. To activate  $\text{CO}_2$  molecules, it is imperative to adjust the surface basicity to improve the adsorption capability towards  $\text{CO}_2$ . To achieve this goal, the effect of introducing various rare earth and other transition metals on catalytic properties in  $\text{CO}_2$  methanation has been extensively studied in past decades. Yan *et al.*<sup>74</sup> demonstrated that W doping can strengthen the Ni–Mg



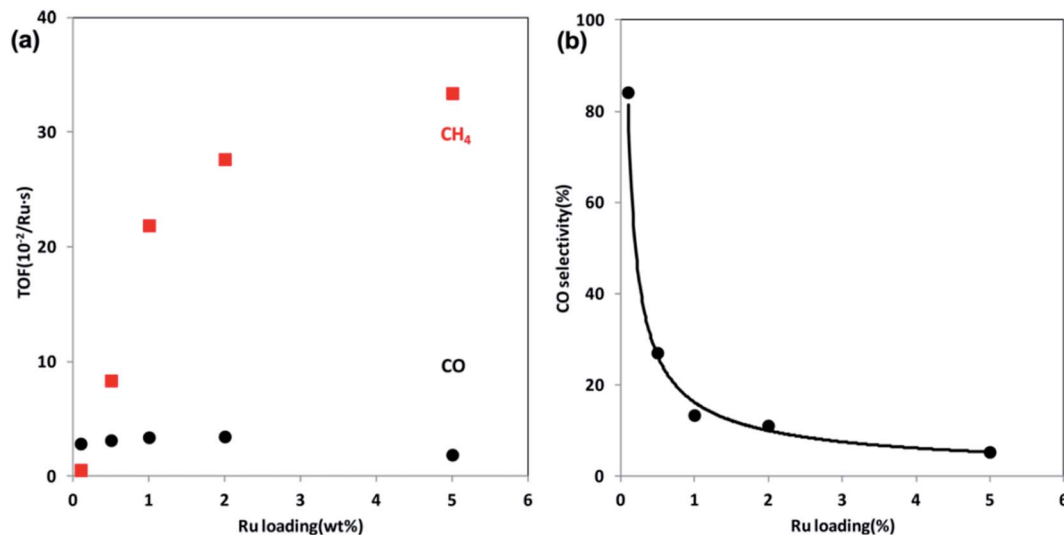


Fig. 6 (a) TOFs of CO and CH<sub>4</sub> formation at steady state at 300 °C over Ru/Al<sub>2</sub>O<sub>3</sub> catalysts as a function of Ru loading. (b) CO selectivity as a function of Ru loading at 300 °C. Reprinted with permission from ref. 47. Copyright 2013 ACS.

interaction, and enhance NiMgO<sub>x</sub> catalytic performance in terms of CO<sub>2</sub> methanation activity and stability. Furthermore, such W doping also increased the surface basic sites of NiMgO<sub>x</sub>, which could improve CO<sub>2</sub> stabilization and its subsequent hydrogenation effectively. DRIFTS analysis further demonstrates that these resultant surface basic sites promoted the transfer of adsorbed CO<sub>2</sub> to monodentate formate species (m-HCOO\*) which was proposed as the key intermediate for the CO<sub>2</sub> methanation.

Similarly, Wierzbicki *et al.*<sup>75</sup> increased the surface basicity by adding 2 wt% lanthanum to Ni-Mg-Al hydrotalcite-derived catalysts, which remarkably enhanced the CO<sub>2</sub> methanation activity. In addition, a series of rare earth-doped (La, Ce, Sm, and Pr) Ni-based mesoporous materials were facilely fabricated by the one-pot evaporation-induced self-assembly strategy for low-temperature CO<sub>2</sub> methanation.<sup>76</sup> The rare earth-doped catalysts with enhanced surface basicity displayed two or three times higher catalytic activities than the pristine MA-10Ni catalyst in the low-temperature region (200–250 °C). Generally speaking, catalyst basicity improvement increases the CO<sub>2</sub> adsorption and activation by the second metal addition.

**2.1.4 Novel catalysts and process integration.** In addition to the traditional metal-support catalysts, more attention has been paid to the incorporation of novel materials with desired features to produce heterogeneous catalysts for CO<sub>2</sub> hydrogenation, such as multi-metal composite oxides, hydrotalcite, perovskite, and metal-organic framework (MOF)-based catalysts. Depending upon the knowledge and experience collected so far, specific novel materials were intentionally chosen for further modification and/or incorporation with active metals that were already identified as active sites. Preliminary results demonstrate that the tailored materials are capable of improving the catalytic performance as anticipated through strengthened metal-support interaction, generated oxygen vacancies, and improved reducibility of metals. In addition, by DFT calculations, the undercoordinated sites (UCSS) serve as

the active centers for hydrogen-assisted CO dissociation and the CO dissociation barrier decreases proportionally with the expansion of the crystal lattice.<sup>77</sup> Recently, by a rapid quenching technique, Zong *et al.*<sup>78</sup> fabricated RQ Ni with peculiar UCS-abundant and tensile-strained structural characteristics. This catalyst has superior activity in the low-temperature CO<sub>2</sub> methanation and the TOF of CO<sub>2</sub> on RQ Ni is about 8 times that of the highest TOF of CO<sub>2</sub> ever reported at 473 K. By DFT calculations, the CO activation barrier decreases when the Ni-Ni distance expanded from 2.49 Å to 2.51 Å with tensile strain on the Ni(111) surface. The superior activity conforms to the conclusion that the UCSs are the active centers for CO<sub>x</sub> methanation and more efforts should be aimed at fabricating undercoordinated catalytic materials.

Centi and co-workers have developed γ-Al<sub>2</sub>O<sub>3</sub>-ZrO<sub>2</sub>-TiO<sub>2</sub>-CeO<sub>2</sub> composite oxide-supported Ni catalysts<sup>79</sup> and Ni-Al hydrotalcite<sup>80</sup> catalysts for CO<sub>2</sub> methanation. A better performance of the catalysts was achieved because of the improvements in the reducibility of active metal Ni.

Metal oxides have relatively low surface areas without featuring pore structures, thereby limiting the intimate contact between reagents and active sites, and even leading to mass transfer limitation. To resolve such issues, some high BET surface supports have been explored. MOFs are a class of crystalline, nanoporous materials that offer such tailorability through large accessible surface areas, tunable pore functionalities, and reactive open metal sites.<sup>81–83</sup> Zhen *et al.*<sup>84</sup> prepared Ni-based catalysts using MOF-5 (surface area of 2961 m<sup>2</sup> g<sup>-1</sup>) as support, and obtained a high Ni dispersion (41.8%). Such 10Ni/MOF-5 catalyst with highly dispersed Ni showed a higher activity than the benchmark Ni/SiO<sub>2</sub>, and presented a superior stability after 100 h on stream for low-temperature CO<sub>2</sub> methanation. Li *et al.*<sup>85</sup> prepared ZIF-67-derived Co-based porous carbon catalysts, and achieved both excellent catalytic performance and good stability in comparison to the traditional Al<sub>2</sub>O<sub>3</sub>-supported counterpart. This catalyst even exhibited



prominent activity performance in CO<sub>2</sub> methanation at low temperatures compared with the other Co-based catalysts supported on either metal oxides or zeolites.<sup>41,42,86</sup> Meanwhile, Zeng *et al.*<sup>87</sup> have proposed a general synthesis route of ZIF-67-derived bifunctional nanoreactors *via* a water-soaking-assisted phase-transformation method for CO<sub>2</sub> hydrogenation. They point out that CO<sub>2</sub> converts to CO on the Pt active sites and CO methanation to CH<sub>4</sub> occurs on the Co active sites. The Pt@CSN (cobalt silicate nanoparticles) bifunctional nanoreactors increase the CO<sub>2</sub> conversion and CH<sub>4</sub> selectivity obviously through prolonging the intermediate retention time on the catalyst surface and enhancing the probability for CO to further convert to CH<sub>4</sub>. These achievements provide insight into adapting these advancements toward the industrial utilization of CO<sub>2</sub> in terms of economic and sustainable viability. However, MOFs are unfavorable for high-temperature reaction because of their instability under the hydrothermal reaction conditions, especially given that CO<sub>2</sub> hydrogenation usually requires high temperature. From another point of view, developing low-temperature methanation catalysts with high activity is also a promising way for CO<sub>2</sub> conversion from the energy conservation perspective.

In addition to the traditional homogeneous catalyst preparation methods, such as impregnation method and coprecipitation method, more and more innovation techniques have been employed to prepare catalytic materials to remedy the defects existing in traditional methods. Kawi and co-workers developed Ni/Ce-ZrO<sub>2</sub> catalysts by the ammonia evaporation (AE) method, and remarkably improved the Ni reducibility (total H<sub>2</sub> uptake = 3.37 mmol g<sup>-1</sup>) compared with the impregnation (total H<sub>2</sub> uptake = 3.32 mmol g<sup>-1</sup>) and deposition-precipitation (total H<sub>2</sub> uptake = 2.06 mmol g<sup>-1</sup>) methods.<sup>88</sup> The Ni/Ce-ZrO<sub>2</sub>-AE possessed more oxygen vacancies, and a strengthened metal-support interaction, thereby contributing to the high activity and stability for low-temperature CO<sub>2</sub> methanation. Schubert *et al.*<sup>89</sup> used the double flame spray pyrolysis technique to control the Pt content to as low as 0.03 wt%, and improved the catalytic performance of PtCo-Al<sub>2</sub>O<sub>3</sub> significantly. Protasova *et al.*<sup>90</sup> manufactured macro-porous catalytic supports by an innovative and highly reproducible robocasting technique, three dimensional fiber deposition (3DFD), and the supports were coated with Ni/Al<sub>2</sub>O<sub>3</sub> suspension to achieve sufficient catalytic coating. The catalysts coated on 3DFD supports had improved mass and heat transfer properties, and prevented metal sintering efficiently. These advantages were conducive to maintain the stability of the catalysts. Liu *et al.*<sup>91</sup> attained a better catalytic performance of Ni/TiO<sub>2</sub> catalysts prepared by dielectric barrier discharge plasma, depending on which more active Ni(111) facets were selectively exposed for CO<sub>2</sub> methanation.<sup>92</sup>

To accord with practical applications, researchers have recently paid attention to the integration of carbon dioxide capture and utilization processes by incorporating together both CO<sub>2</sub> capture system and catalytic CO<sub>2</sub> conversion system. Farrauto<sup>8,93</sup> and co-workers devoted their effort to exploring dual functional catalysts which enable CO<sub>2</sub> capture from an emission source, and conversion of it to synthetic natural gas in

the same reactor at the same temperature (320 °C). In this process, the catalyst composition comprised 5% Ru 10% CaO/Al<sub>2</sub>O<sub>3</sub>, wherein the components of CaO and Ru were responsible for CO<sub>2</sub> adsorption and conversion, respectively. Of note, this new approach utilized flue gas sensible heat, and needed no additional heat input, which made it more attractive in mitigating the current energy shortage. Grunwaldt *et al.*<sup>33</sup> explored Ni-based catalysts under dynamic reaction conditions, especially under a fluctuating supply of renewable H<sub>2</sub>. They found the oxidation of Ni particles occurred after the removal of H<sub>2</sub> from the gas stream, and a lower catalytic performance was observed consequently. Apparently, the Ni/CaO-Al<sub>2</sub>O<sub>3</sub> catalyst was unadapted to the dynamic reaction conditions. Such an issue impeded its implementation in real industry, which also made the search for efficient ways for renewable H<sub>2</sub> supply more important.

## 2.2 Mechanisms of CO<sub>2</sub> methanation

CO<sub>2</sub> methanation can be catalyzed through either CO route or formate route, which is determined by the properties of different active metals and supports. The CH<sub>4</sub> selectivity is likely determined by the competition between the hydrogenation and C-O bond scission reactions of the \*H<sub>x</sub>CO intermediates. To achieve high CH<sub>4</sub> selectivity, the binding of \*H<sub>x</sub>CO species should be strong enough to facilitate C-O bond cleavage.<sup>61</sup>

Duan *et al.*<sup>96</sup> investigated the effect of oxygen vacancies on the catalytic performance of Rh/CeO<sub>2</sub> catalysts in CO<sub>2</sub> methanation, and developed an understanding of its role in the proposed mechanism. The existence of Ce<sup>3+</sup>, surface hydroxyl, and oxygen vacancies on Ru/CeO<sub>2</sub> was evidenced from operando XANES, IR, and Raman analyses. Steady-state isotope transient kinetic analysis (SSITKA)-type *in situ* DRIFTS was employed to detect the surface intermediates and track their transformation during the reaction process on both Ru/CeO<sub>2</sub> and Ru/Al<sub>2</sub>O<sub>3</sub>, wherein the latter was introduced as reference, as it barely had any oxygen vacancies. On the Ru/Al<sub>2</sub>O<sub>3</sub> catalyst, the carbonyl species, originating from the chemisorbed CO\*, was observed until 250 °C, and CH<sub>4</sub> generation occurred within the same temperature range. In contrast, formate and methanol corresponding bands emerged for Ru/CeO<sub>2</sub>, in which the former was identified as a key intermediate *via* this route, and methanol-to-methane transformation was the rate-determining step at a much lower temperature (150 °C). In this work, oxygen vacancies played a crucial role in CO<sub>2</sub> activation and formate formation. Sharma *et al.*<sup>97</sup> prepared Ru-substituted Ce<sub>0.95</sub>Ru<sub>0.05</sub>O<sub>2</sub> catalyst for CO<sub>2</sub> methanation, and interpreted a plausible reaction mechanism by combining the characterization results (TPR and DRIFTS) and DFT calculation. In this case, surface CO\* species, rather than formate, was more likely to act as a key intermediate for CH<sub>4</sub> production, wherein the reaction proceeded through the following steps: CO<sub>2</sub> → CO → OCH<sub>2</sub> → OCH<sub>3</sub> → CH<sub>4</sub>. Note that this proposed reaction pathway differed from that of the supported metal catalyst (Ru/CeO<sub>2</sub>), which proceeded *via* CO<sub>2</sub> → CO → HCOO<sup>-</sup> → C → CH<sub>4</sub>.

Ren *et al.*<sup>92</sup> investigated the mechanisms of CO<sub>2</sub> methanation on Ni(111) surfaces by DFT through three routes with



and without CO formation (Fig. 7). Considering the energy barriers and reaction energies for these different routes, the CO route was more favorable energetically for CO<sub>2</sub> methanation on Ni(111) surface: CO<sub>2</sub> → CO + O → C + O + 4H → CH<sub>2</sub> + 2H → CH<sub>3</sub> + H → CH<sub>4</sub>. Salmeron *et al.*<sup>98</sup> also concluded that the methanation reaction proceeded *via* CO intermediate on Ni(111) surface as evidenced by ambient pressure X-ray photoelectron spectroscopy. Meanwhile, they reported that the Ni(110) seemed to convert CO much more easily to atomic carbon than Ni(111). Henriques *et al.*<sup>18</sup> also investigated the mechanism of USY zeolites-supported Ni catalysts for CO<sub>2</sub> methanation, and reported results also supporting the CO route. On the other hand, Gonzalez *et al.*<sup>99</sup> identified the surface species on Ni/ZrO<sub>2</sub> catalysts and bare ZrO<sub>2</sub> during CO<sub>2</sub> methanation using DRIFTS, and they proposed a different scenario with the formate route as the favorable one, as displayed in Fig. 8. In this mechanism, chemisorbed CO<sub>2</sub> reacted with surface hydroxyl groups of ZrO<sub>2</sub> to give bicarbonate species that can be reversibly converted to carbonate species. H<sub>2</sub> was dissociated on the surface of Ni particles, which may migrate to the reducible metal oxide support by a spillover process, resulting in the formation of surface hydroxyl groups, metal-H species, and formate species. Next, the formate species took part in further hydrogenation to form CH<sub>4</sub>.

In contrast to other reports,<sup>18,92</sup> the Ni/ZrO<sub>2</sub> catalysts barely presented vibrational bands of carbonyl species on Ni surface. Instead, carbonate and bicarbonate species were identified on both Ni/ZrO<sub>2</sub> and bare ZrO<sub>2</sub>, and even their subsequent transition to formate species was evidenced. Clearly, the incorporation of Ni and ZrO<sub>2</sub> was characteristic of bifunctionality for CO<sub>2</sub> methanation, in which the former metal sites were responsible for providing hydrogen through dissociation, while the latter support accounted for the CO<sub>2</sub> stabilization and activation. In other words, CO<sub>2</sub> methanation can be catalyzed through the formate route rather than the CO route on ZrO<sub>2</sub>-supported Ni catalysts.

In sum, the reaction pathway of CO<sub>2</sub> methanation varied depending on the catalytic system used, and strongly depended on the selection of active metals and supports and their interactions.

### 2.3 Deactivation of CO<sub>2</sub> methanation catalysts

Deactivation of metal catalysts is a big challenge in CO<sub>2</sub> methanation. The deactivation of methanation catalysts can be divided into two types: (a) chemical deactivation and (b) physical deactivation.

The chemical deactivation of CO<sub>2</sub> methanation catalysts is mainly directed toward the decrease of active sites caused by the formation of spinel structure. Li *et al.*<sup>62</sup> prepared Co/ZrO<sub>2</sub> catalysts for CO<sub>2</sub> methanation, as well as Co/Al<sub>2</sub>O<sub>3</sub> catalysts for comparison. The Co/ZrO<sub>2</sub> catalysts displayed a higher CO<sub>2</sub> methanation activity with a practically stable performance even after 300 h on stream, while the Co/Al<sub>2</sub>O<sub>3</sub>, in contrast, deactivated rapidly within the same period of time. The deactivation of the Co/Al<sub>2</sub>O<sub>3</sub> catalyst was further studied through thermogravimetric analysis and hydrothermal (H<sub>2</sub>O) treatment verification tests. Extra H<sub>2</sub>O was pumped into the reaction system which led to a large amount of CoAl<sub>2</sub>O<sub>4</sub> being formed and accelerated the Co/Al<sub>2</sub>O<sub>3</sub> catalyst deactivation. Thus, the product H<sub>2</sub>O promotes the formation of the inactive phase CoAl<sub>2</sub>O<sub>4</sub>, leading to the rapid deactivation of Co/Al<sub>2</sub>O<sub>3</sub> catalysts. Carbon deposition is one of the reasons for deactivation; however, the main reason for deactivation is the formation of inactive phase CoAl<sub>2</sub>O<sub>4</sub> spinel structure.

Physical deactivation is caused by carbon deposition and active metal sintering. Kesavana *et al.*<sup>100</sup> synthesized Ni/YSZ catalysts by different methods. On the Ni/YSZ catalyst obtained by impregnation method, graphitic filaments are formed on Ni<sup>0</sup> particles exposing flat surfaces, whereas thin layers of carbon are formed on Ni<sup>0</sup> particles with spherical shape. Ni/YSZ(EDTA) catalyst showed remarkable stability and operando XAS showed that Ni/YSZ(EDTA) catalyst did not undergo deactivation by Ni<sup>0</sup> → Ni<sup>2+</sup> oxidation using high CO<sub>2</sub> : H<sub>2</sub> ratio. Carbon deposition on the catalyst can be avoided by adding steam or increasing the H<sub>2</sub>/CO<sub>2</sub> ratio because hydrogen reacts with the carbon deposits and prevents catalyst deactivation. To mitigate metal sintering, common strategies are increasing metal dispersion through strong metal-support interaction,<sup>62</sup> adding catalyst promoters,<sup>101</sup> and developing advanced synthesis methods.<sup>89</sup> Li *et al.*<sup>85</sup> prepared MOF-derived Co-based porous carbon catalysts in which the active Co particles are separated by the graphite-like carbon avoiding metal sintering

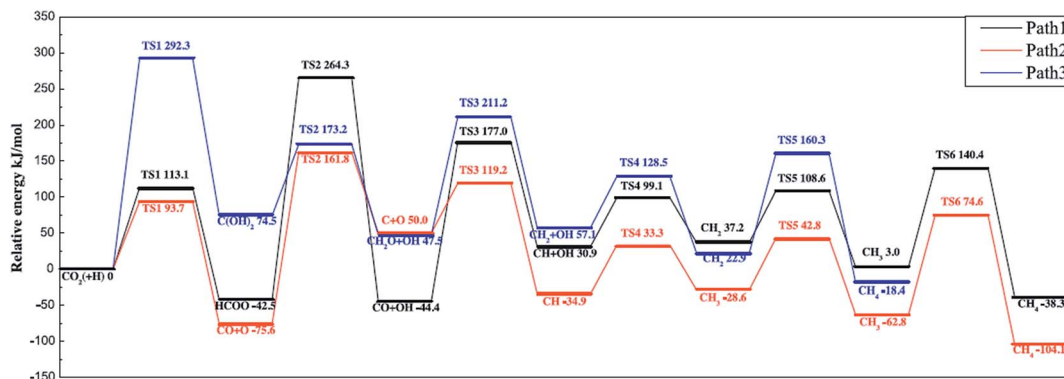


Fig. 7 Potential energy diagram of three mechanisms of CO<sub>2</sub> methanation. Reprinted with permission from ref. 92. Copyright 2015 Elsevier.





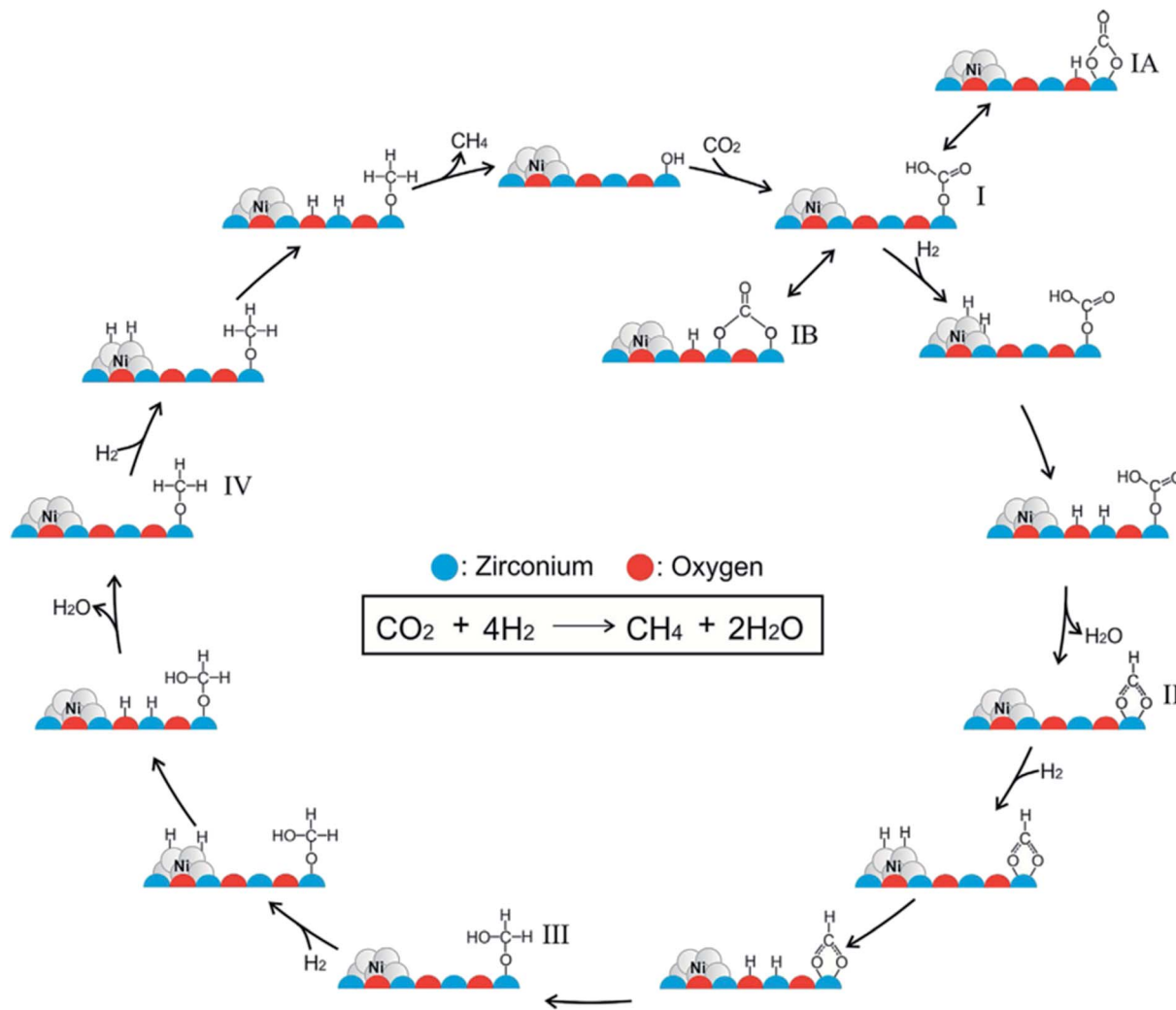


Fig. 8 Mechanism of CO<sub>2</sub> methanation on ZrO<sub>2</sub>-supported Ni catalysts. Reprinted with permission from ref. 99. Copyright 2017 Elsevier.

effectively. A special catalyst structure can also resist metal sintering effectively. Li *et al.*<sup>94</sup> prepared NiO–MgO@SiO<sub>2</sub> core-shell structured catalysts, and activity performance was successfully retained after 100 h on stream. In summary, particles with appropriate size are beneficial for CH<sub>4</sub> formation.

### 3. CO<sub>2</sub> hydrogenation to C<sub>2+</sub> hydrocarbons

CO<sub>2</sub> hydrogenation to C<sub>2+</sub> hydrocarbons is of great importance because the long-chain hydrocarbons possess higher energy density, and could be used as fuels and chemicals for a wide range of applications. Utilizing CO as the carbon source for hydrocarbon synthesis through Fischer–Tropsch synthesis has been widespread in industry, and continuing studies to further improve the activity, tune the product distribution, and develop deep understandings of catalytic composition–performance–physicochemical relationships are still ongoing worldwide.<sup>102,103</sup> Substituting CO with CO<sub>2</sub> as carbon source makes the reaction thermodynamically more difficult (see the reaction

enthalpy below).<sup>104</sup> Besides, not only will the challenge originate from the chemical inertness of CO<sub>2</sub>, but also from the competition with CO<sub>2</sub> methanation.<sup>73</sup> The relatively small amount of CO<sub>2</sub> adsorbed species compared with dissociated H\* on a catalyst surface leads to a low C/H ratio, which favors the fast hydrogenation of surface-adsorbed intermediates and the formation of methane and prevents chain growth.<sup>12,56,105</sup> Despite the difficulties, the transformation of CO<sub>2</sub> to value-added chemicals still receives great attention worldwide because of the significance in providing sustainable alternatives to solve urgent issues such as those of energy and the environment. This section will discuss the most recent advances in CO<sub>2</sub> hydrogenation to hydrocarbons. Similarly, some representative catalysts for CO<sub>2</sub> hydrogenation to C<sub>2+</sub> hydrocarbons are presented in Table 2.

#### 3.1 Modified Fischer–Tropsch synthesis (FTS) route

Primarily, CO<sub>2</sub> hydrogenation to hydrocarbons could proceed through both direct and indirect pathways. The direct way is straightforward conversion of CO<sub>2</sub> to hydrocarbons<sup>106</sup> (eqn (1))



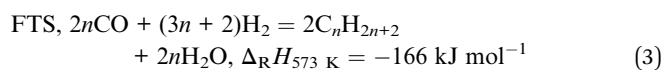
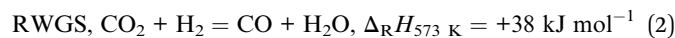
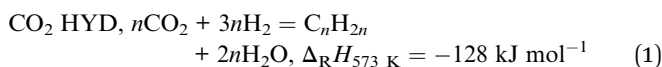
Table 2 Summary of various catalysts for CO<sub>2</sub> hydrogenation to C<sub>2+</sub> hydrocarbons

| Catalyst  | Preparation method             | GHSV<br>[mL h <sup>-1</sup> g <sup>-1</sup> ] | P<br>[MPa] | T<br>[°C] | X <sub>CO<sub>2</sub></sub><br>[%] | S <sub>CO</sub><br>[%] | S <sub>CH<sub>4</sub></sub><br>[%] | S <sub>C<sub>2</sub>-C<sub>4</sub></sub><br>[%] | S <sub>C<sub>5+</sub></sub><br>[%] | O/P  | Ref. |
|---|--------------------------------|---|------------|-----------|------------------------------------|------------------------|------------------------------------|---|------------------------------------|------|------|
| Fe <sub>2</sub> O <sub>3</sub> -CT600             | Precipitation method           | 1140  | 0.15       | 350       | 40.0                               | 15 <sup>a</sup>        | 12 <sup>a</sup>                    | 37 <sup>a</sup>                                 | 36 <sup>a</sup>                    | 2.7  | 112  |
| 20% Fe/cube-CeO <sub>2</sub>                      | Incipient wetness impregnation | 200   | —          | 390       | 18.9                               | 73.5 <sup>a</sup>      | 75.5 <sup>b</sup>                  | 22.2 <sup>b</sup>                               | 1.9 <sup>b</sup>                   | 4.1  | 115  |
| Fe-Co(0.17)/K(1.0)/Al <sub>2</sub> O <sub>3</sub> | Incipient wetness impregnation | 3600  | 1.1        | 300       | 31.0                               | 18 <sup>a</sup>        | 13 <sup>a</sup>                    | 69 <sup>a</sup>                                 | —                                  | —    | 116  |
| 10K13Fe2Co100ZrO <sub>2</sub>                     | Electro-spinning method        | 3600  | 3          | 400       | 42.3                               | 21.9 <sup>a</sup>      | 25.7 <sup>a</sup>                  | 34 <sup>a</sup>                                 | 18.4 <sup>a</sup>                  | 4.2  | 117  |
| CeO <sub>2</sub> -Pt@mSiO <sub>2</sub> -Co        | Hydrothermal and impregnation  | 50 400  | 0.6        | 250       | 2.0                                | 78.0                   | 60.0 <sup>b</sup>                  | 40.0 <sup>b</sup>                               | 0 <sup>b</sup>                     | —    | 118  |
| Delafossite-CuFeO <sub>2</sub>                    | Hydrothermal method            | 1800  | 1          | 300       | 16.7                               | 31.4 <sup>a</sup>      | 2.4 <sup>b</sup>                   | 32.7 <sup>b</sup>                               | 64.9 <sup>b</sup>                  | 7.7  | 119  |
| 0.05MnFe  | One-step sol-gel process       | 6000  | 0.1        | 340       | 30                                 | 7.7 <sup>a</sup>       | 29.3 <sup>b</sup>                  | 67.1 <sup>b</sup>                               | —                                  | 0.37 | 120  |
| ZnGa <sub>2</sub> O <sub>4</sub> /SAPO-34         | Physical mixing                | 5400  | 2          | 370       | 13                                 | 46 <sup>a</sup>        | 1 <sup>b</sup>                     | 97 <sup>b</sup>                                 | 2 <sup>b</sup>                     | 7.8  | 121  |
| ZnZrO/SAPO-34                                     | Physical mixing                | 3600  | 2          | 380       | 12.6                               | 47 <sup>a</sup>        | 3 <sup>b</sup>                     | 94 <sup>b</sup>                                 | 3 <sup>b</sup>                     | 5.7  | 122  |
| In <sub>2</sub> O <sub>3</sub> /HZSM-5            | Granule stacking               | 9000  | 3          | 340       | 13.1                               | 45 <sup>a</sup>        | 1 <sup>b</sup>                     | 13.1 <sup>b</sup>                               | 78.6 <sup>b</sup>                  | —    | 26   |
| In-Zr/SAPO-34                                     | Physical mixing                | 9000  | 3          | 400       | 35                                 | 75 <sup>a</sup>        | 5 <sup>b</sup>                     | 93 <sup>b</sup>                                 | 3 <sup>b</sup>                     | 6.1  | 123  |
| Na-Fe <sub>3</sub> O <sub>4</sub> /HZSM-5         | Granule mix-in                 | 4000  | 3          | 320       | 33.6                               | 14.2 <sup>a</sup>      | 7.9 <sup>b</sup>                   | 18.4 <sup>b</sup>                               | 73.7 <sup>b</sup>                  | —    | 105  |
| Fe-Zn-Zr@HZSM-5-Hbeta                             | Cladding method                | 3000  | 8          | 340       | 14.9                               | 38.6 <sup>a</sup>      | 1.5 <sup>a</sup>                   | 71.7 <sup>a</sup>                               | 26.8 <sup>a</sup>                  | —    | 124  |
| Cu-Zn-Al/modified-HB                              | Physical mixing                | 1500  | 0.98       | 300       | 27.6                               | 53.4 <sup>a</sup>      | 0.7 <sup>a</sup>                   | 43.2 <sup>a</sup>                               | 2.3 <sup>a</sup>                   | —    | 125  |

<sup>a</sup> Calculated from equation  $S_i(\%) = \frac{m_i n_{i,\text{out}}}{n_{\text{CO}_2,\text{in}} - n_{\text{CO}_2,\text{out}}} \times 100\%$ , where  $n_{\text{CO}_2,\text{in}}$  and  $n_{\text{CO}_2,\text{out}}$  represent the molar concentration of CO<sub>2</sub> in the feed and effluent, respectively;  $n_{i,\text{out}}$  represents the molar concentration of product  $i$  in the effluent; and  $m_i$  represents the number of carbon atoms in product  $i$ . Products include CO and hydrocarbons. <sup>b</sup> Calculated from equation:

$$C_i \text{ hydrocarbon selectivity}(\%) = \frac{\text{mole of } C_i \text{ hydrocarbon} \times i}{\sum_{i=1}^n \text{mole of } C_i \text{ hydrocarbon} \times i} \times 100\%.$$

or going through the RWGS reaction and FTS reaction (eqn (2) and (3)).<sup>107,108</sup> In addition to these proposed reaction pathways, some scientists have also attempted to use methanol as a bridge and building unit to synthesize long-chain hydrocarbons *via* CO<sub>2</sub> hydrogenation, and made a major breakthrough most recently.<sup>96</sup> This newly developed reaction pathway is another alternative option for CO<sub>2</sub> hydrogenation to hydrocarbons through an indirect way.



Since converting CO<sub>2</sub> to hydrocarbons directly makes the reaction kinetically more difficult,<sup>104</sup> some scientists have turned to the modified FTS route. This section will mainly focus on the major progress made in CO<sub>2</sub> hydrogenation to C<sub>2+</sub> hydrocarbons through the modified FTS route. Currently, FTS is mainly catalyzed by Fe-based catalysts because the metal Fe possesses the catalytic characteristic of improving C-C coupling, which was proposed as a rate-determining step.<sup>109</sup> In 1978, Dwyer *et al.*<sup>110</sup> found that the presence of CO<sub>2</sub> impacted the product distribution of FTS on Fe-based catalysts, and such an inspired finding exploited a new field for the development of active catalysts for hydrocarbon synthesis from CO<sub>2</sub>, an alternative carbon source with even greater proportion in the atmosphere. Computational results demonstrate that the kinetics of FTS is not comparable to that of RWGS, which makes

it another challenge other than carbon chain growth.<sup>111</sup> Even so, the similarity between CO and CO<sub>2</sub> hydrogenation motivated people to apply Fe catalysts, which exhibited good performance in FTS, to CO<sub>2</sub> hydrogenation at an early stage, and more researchers then endeavored to apply modified Fe catalysts with desired features. Albrecht *et al.*<sup>112</sup> prepared dopant-free bulk Fe<sub>2</sub>O<sub>3</sub> by a cellulose-template (CT) synthesis method, and applied it in CO<sub>2</sub> hydrogenation to hydrocarbons. The catalysts selectively catalyze CO<sub>2</sub> to C<sub>2</sub>-C<sub>4</sub> hydrocarbons (selectivity = 37%) with an olefin to paraffin (O/P) ratio of 2.7. Iron carbide, as high as 81 wt%, was detected on the spent Fe<sub>2</sub>O<sub>3</sub>-CT600 catalysts, which was considered as active sites for the FTS.<sup>113,114</sup> In comparison to FTS, this CT-supported Fe<sub>2</sub>O<sub>3</sub> catalyst yielded comparable C<sub>2</sub>-C<sub>4</sub> hydrocarbons, which could be attributed to the improved reducibility and *in situ* formation of iron carbide promoted by the CT-synthesized catalyst precursor.

**3.1.1 Selection of support materials.** As is well known, the incorporation of a support is able to tune the dispersion of active sites depending on the metal-support interaction. Due to its featured surface chemistry and amphoteric property, Al<sub>2</sub>O<sub>3</sub> might have a strong interaction with loaded metallic species, and was widely used as support material for the preparation of commercially available catalyst for methanol synthesis.<sup>126</sup> To increase the Fe dispersion, Al<sub>2</sub>O<sub>3</sub> was also employed as a support in the preparation of Fe catalysts for CO<sub>2</sub> hydrogenation to hydrocarbons. Ding *et al.*<sup>127</sup> prepared a series of FeK/Al<sub>2</sub>O<sub>3</sub> catalysts, and investigated the effect of surface hydroxyl groups of Al<sub>2</sub>O<sub>3</sub> on the activity and selectivity of hydrocarbon synthesis *via* CO<sub>2</sub>. Evidently, the variations of both Fe dispersion and particle size were strongly dependent on the point of zero charge (PZC) of the Al<sub>2</sub>O<sub>3</sub> support. The Fe



dispersion increased monotonically with the increase of PZC value, while the particle size showed an opposite trend. The highest CO<sub>2</sub> conversion (54.4%) and selectivity of C<sub>5+</sub> hydrocarbons (31.1%) were achieved at PZC = 8.0. ZrO<sub>2</sub> (ref. 128) and CeO<sub>2</sub> (ref. 63 and 88) were used as support materials as well due to the basic sites and the oxygen vacancies.<sup>96</sup> Wang *et al.*<sup>129</sup> carried out screening tests on catalysts prepared with different types of support materials, including SiO<sub>2</sub>, Al<sub>2</sub>O<sub>3</sub>, TiO<sub>2</sub>, ZrO<sub>2</sub>, mesoporous carbon, and carbon nanotubes (CNTs), among which ZrO<sub>2</sub> attained the highest selectivity and yield for lower olefins. Chew *et al.*<sup>108</sup> used N-doped CNTs as a support to prepare Fe-based catalysts (Fe/NCNTs), and O-doped CNT- and SiO<sub>2</sub>-supported catalysts were also employed for comparison. Characterization results demonstrate that the incorporation of NCNTs greatly improved the Fe dispersion and reducibility, which benefited from the improved hydrophilicity and appropriate metal-support interaction. On the other hand, the O-doped SiO<sub>2</sub> support showed too strong an interaction with the Fe species, which, in turn, exhibited a negative impact on the reducibility of active metal. Murciano *et al.*<sup>115</sup> prepared Fe catalysts by introducing CeO<sub>2</sub> with various morphological properties, and examined their influence on the activity and selectivity in CO<sub>2</sub> hydrogenation to hydrocarbons. Results showed a strong reliance of catalytic performance on the reducibility of Fe species on the support. Among those CeO<sub>2</sub> materials, the one with cubic morphology helped to improve the reducibility of Fe species as evidenced from the shift of the initial reduction temperature towards lower temperatures, thereby resulting in the obtained highest O/P ratio in comparison to rod-type and nanoparticle-type CeO<sub>2</sub>.

Owing to their tailorable pore structure and featured physicochemical properties, MOFs and their subclass zeolitic imidazolate frameworks (ZIFs) have attracted considerable attention in a diversity of energy-related applications such as CO<sub>2</sub> capture and even CO<sub>2</sub> activation.<sup>130–132</sup> Driven by their unique characteristic, researchers employed this group of materials as supports to prepare heterogeneous catalysts for CO<sub>2</sub> hydrogenation to hydrocarbons.<sup>84,133</sup> Some metal-based MOFs and ZIFs, which already were proven to be active for hydrocarbon synthesis from either CO<sub>2</sub> or CO hydrogenation, were selectively chosen for activity tests in an attempt to collect first-hand data. Guo and coworkers proposed and carried out a series of tests using these novel catalysts, and obtained interesting results. In an early work, they employed MIL-53(Al) and ZIF-8 as supports for preparing α-Fe<sub>2</sub>O<sub>3</sub> catalysts by a solid grinding method.<sup>133</sup> Preliminary results indicated that ZIF-8-supported catalysts exhibited a higher CO<sub>2</sub> conversion than MIL-53-supported ones because the acidity on the MIL-53 impeded CO<sub>2</sub> adsorption, an important step for heterogeneous catalysis.

**3.1.2 Incorporation of promoters in Fe-based catalysts.** To further improve the selectivity of higher hydrocarbons, Fe-based catalysts were promoted by a variety of metals, among which K, Na, Cs, Mn, and Cu were representative ones, enabling the enhancement not only of C<sub>2+</sub> selectivity, but also CO<sub>2</sub> conversion. Wang *et al.*<sup>129</sup> added alkali metal ions (with the exception of Li<sup>+</sup>) to Fe/ZrO<sub>2</sub> catalysts. Among Na<sup>+</sup>, K<sup>+</sup>, and Cs<sup>+</sup>,

(0.5–1.0 wt%)K(10 wt%)Fe/ZrO<sub>2</sub> exhibited the highest CO<sub>2</sub> conversion. Satthawong *et al.*<sup>116</sup> investigated the effect of K addition on light olefin production from CO<sub>2</sub> hydrogenation over Al<sub>2</sub>O<sub>3</sub>-supported Fe–Co bimetallic catalysts. When the K/Fe atomic ratio was 1, the Fe–Co bimetallic catalysts yielded the highest amount of C<sub>2</sub>–C<sub>4</sub> olefins. Detailed temperature-programmed desorption (TPD) analyses demonstrate that the K<sub>2</sub>O on the surface behaved in a manner to suppress the adsorption towards weakly bonded hydrogen which appeared to correlate with the formation of methane. Moreover, the addition of K was able to increase the basicity of the surface, through which more adsorption sites were created on the surface. In other words, the K promoter was capable of shifting the selectivity from methane to desired higher hydrocarbons by tuning the surface H/C ratios. Wei *et al.*<sup>134</sup> studied the effect of sodium on iron-based catalysts in the CO<sub>2</sub> hydrogenation process. They reported that sodium can promote the surface basicity of catalysts, which was beneficial for CO<sub>2</sub> adsorption and the carbonization of Fe<sub>3</sub>O<sub>4</sub>, leading to more C<sub>2</sub>–C<sub>4</sub> olefins (46.6%) and C<sub>5+</sub> hydrocarbons (30.1%). Combining the knowledge and experience accumulated, the same group made an exciting breakthrough in CO<sub>2</sub> conversion to gasoline fuels.<sup>105</sup> Inspired by the methanol-to-gasoline process and various applications of zeolite in hydrocarbon-related<sup>105</sup> oligomerization, the Na–Fe<sub>3</sub>O<sub>4</sub>/HZSM-5 catalyst was prepared with the characteristic of selectively producing gasoline components (78%) over methane (4%) of all hydrocarbons at 22% CO<sub>2</sub> conversion. Characterization results indicate the newly developed catalyst worked in a multifunctional manner, wherein Na, Fe<sub>3</sub>O<sub>4</sub>, Fe<sub>5</sub>C<sub>2</sub>, and acid sites on zeolites were responsible for surface basicity, RWGS, FTS, and oligomerization to hydrocarbons, respectively (Fig. 9). More importantly, instead of functioning separately, granule-mixed catalysts gave a maximum gasoline component selectivity, indicating that selectivity is a function of proximity of the active species. Fierro *et al.*<sup>120</sup> prepared a series of manganese-iron oxide catalysts with different Mn contents, and found the 0.05MnFe catalyst exhibited the highest CO<sub>2</sub> conversion and C<sub>2</sub>–C<sub>5</sub> selectivity. The enhanced activity mainly resulted from the improved reducibility and the Mn-induced promotion of RWGS and FTS reactions. Choi *et al.*<sup>119</sup> developed a new catalyst prepared by reduction of delafossite-CuFeO<sub>2</sub> and the catalyst can be

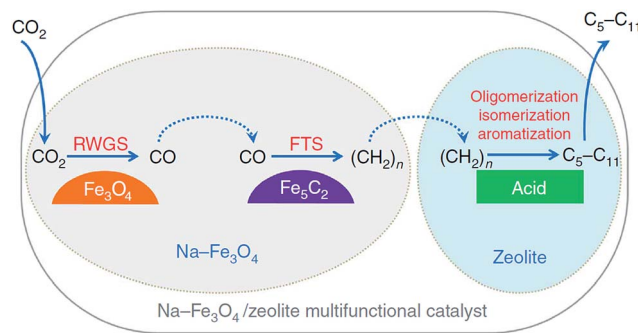


Fig. 9 Reaction scheme for CO<sub>2</sub> hydrogenation to gasoline-range hydrocarbons through modified FTS route. Reprinted with permission from ref. 105. Copyright 2017 Nature.



transformed *in situ* to active phase  $\chi$ -Fe<sub>5</sub>C<sub>2</sub>. The CuFeO<sub>2</sub>-derived catalyst selectively generated 65% C<sub>5+</sub> hydrocarbons with 16.7% CO<sub>2</sub> conversion, while the reference catalysts derived from bare Fe<sub>2</sub>O<sub>3</sub>, namely CuO–Fe<sub>2</sub>O<sub>3</sub> mixture and spinel CuFe<sub>2</sub>O<sub>4</sub>, were much less active, and mainly produced light hydrocarbons.

**3.1.3 Other metal-based strategies.** Fe and Co both display excellent performances in FTS, but Co-based catalysts selectively produce methane when replacing CO with CO<sub>2</sub> as carbon source.<sup>135</sup> Lietti *et al.*<sup>136</sup> developed a deep understanding of the difference between CO and CO<sub>2</sub> hydrogenation on Co- and Fe-based catalysts. They found that the different adsorption strengths of CO and CO<sub>2</sub> affected the H/C ratio on different catalyst surfaces, wherein CO<sub>2</sub> was more active than CO on Co than Fe. If CO<sub>2</sub> hydrogenation goes through the CO-mediated route, the abundance of chemisorbed CO\* is a prerequisite and the Co-based catalysts are the ideal ones.

Yang *et al.*<sup>118</sup> prepared CeO<sub>2</sub>–Pt@mSiO<sub>2</sub>–Co core-shell catalysts for converting CO<sub>2</sub> to C<sub>2</sub>–C<sub>4</sub> hydrocarbons. The two interfaces of Pt–CeO<sub>2</sub> and Co–SiO<sub>2</sub> were intentionally created depending on the unique core-shell structure, wherein the former accounted for converting CO<sub>2</sub> to CO through RWGS, while the latter accounted for the subsequent hydrogenation to C<sub>2</sub>–C<sub>4</sub> through FTS. Notably, this novel catalyst yielded 60% of C<sub>2</sub>–C<sub>4</sub> hydrocarbons in total carbon-containing products except CO (Fig. 10).

Another promising strategy to improve the yield of higher hydrocarbons is the application of bimetallic synergy. Satthawong and coworkers<sup>137</sup> conducted comprehensive screening tests over Fe–M/Al<sub>2</sub>O<sub>3</sub> (M = Co, Ni, Cu, and Pd) catalysts with fixed M/(M + Fe) atomic ratios at 0.1 at per at and their K-promoted counterparts. The combination of Fe with either Co, Cu, or Pd led to a significant improvement of chain-growth possibility and bimetallic promoting effect on C<sub>2+</sub> hydrocarbon formation, while the Fe–Ni(0.1) catalysts, on the contrary, selectively produced undesired CH<sub>4</sub>. Interestingly, the combination of Fe and Co, Cu or Pd enhanced the catalyst activity obviously compared with their monometallic counterparts, indicating a strong synergetic effect and intimate proximity

existed between the combined metal components. Also, the K addition further increased the CO<sub>2</sub> conversion and the C<sub>2</sub>–C<sub>4</sub> olefin production. In following work, the Fe–Co bimetallic catalysts with a wide range of Co/(Fe + Co) atomic ratios (*i.e.*, 0.0–1.0 at per at) were selectively chosen for a systematic examination to unveil the synergetic regime of this bimetallic combination and the function of promoter in terms of adsorption properties.<sup>116,138</sup> Evidently, doping Fe with appropriate amount of Co (*e.g.*, Co/(Co + Fe) = 0.17 mol mol<sup>−1</sup>) can maximize the promotion of C<sub>2+</sub> hydrocarbon production. Inspired by such significant bimetallic synergetic effect, Li *et al.*<sup>117</sup> synthesized Fe–Co–Zr polymetallic fibers for CO<sub>2</sub> hydrogenation, and obtained 27.5% C<sub>2</sub>–C<sub>4</sub> olefins with the addition of K.

### 3.2 Methanol-mediated route

In addition to these proposed reaction pathways, some scientists also attempted to use methanol as a bridge and building unit to synthesize long-chain hydrocarbons *via* CO<sub>2</sub> hydrogenation, and made a major breakthrough most recently.<sup>96</sup> This newly developed reaction pathway is another alternative option for CO<sub>2</sub> hydrogenation to hydrocarbons through an indirect way.

The products of FTS generally follow a statistical hydrocarbon distribution, which is known as the Anderson–Schulz–Flory (ASF) distribution.<sup>139</sup> In the ideal case, the chain-growth probability ( $\alpha$ ) is independent of carbon chain length. Therefore the product distribution is determined by the chain-growth probability ( $\alpha$ ). For example, if CO<sub>2</sub> hydrogenation is through the modified FTS route, ASF distribution of FTS products limits the maximum selectivities of C<sub>5</sub>–C<sub>11</sub> (gasoline range) and C<sub>12</sub>–C<sub>20</sub> (diesel range) hydrocarbons to roughly 45% and 30%, respectively.<sup>140,141</sup> To break the limitation of ASF distribution and get more gasoline or lower olefins, the methanol-mediated route is an ideal path. Enlightened by the superior selectivity to methanol (*ca.* 100%) on In<sub>2</sub>O<sub>3</sub>-based catalysts from CO<sub>2</sub> hydrogenation,<sup>142</sup> Sun *et al.*<sup>26</sup> used In<sub>2</sub>O<sub>3</sub>/HZSM-5 composite to selectively produce 78.6% C<sub>5</sub>–C<sub>11</sub> hydrocarbons with a high octane number through the methanol route, and broke the ASF restraint. In the proposed reaction pathway, CO<sub>2</sub> first was converted to methanol on the In<sub>2</sub>O<sub>3</sub> surface, which was further transformed to hydrocarbons on HZSM-5 *via* the hydrocarbon-pool mechanism. DFT calculation indicates that the CO<sub>2</sub> was first chemisorbed on the oxygen vacancies on the In<sub>2</sub>O<sub>3</sub>, and the active site was not the metallic phase. Fujiwara *et al.*<sup>125</sup> prepared composite catalysts obtained by the physical mixing of Cu–Zn–Al oxide and HB zeolite that was modified with 1,4-bis(hydroxydimethylsilyl)benzene, which were very effective for the production of C<sub>2+</sub> hydrocarbons, and reached *ca.* 12.6% at 300 °C and 0.98 MPa. They proposed a reaction scheme of CO<sub>2</sub> hydrogenation over the composite catalyst as illustrated in Fig. 11. The methanol was synthesized on the Cu–Zn–Al oxide catalyst, and methanol was converted to C<sub>2+</sub> hydrocarbons on the zeolite, which proceeded simultaneously in a single catalytic bed. The preservation of the strong acid sites of the modified HB zeolite with hydrophobic surface improved the second-step CH<sub>3</sub>OH conversion activity.<sup>143</sup>

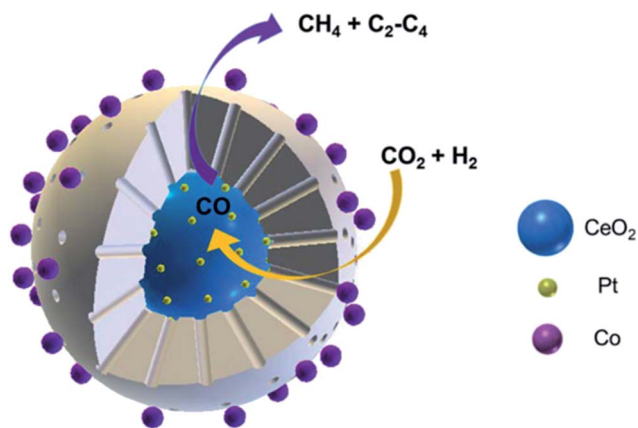


Fig. 10 Schematic diagram of CO<sub>2</sub> hydrogenation on CeO<sub>2</sub>–Pt@mSiO<sub>2</sub>–Co core-shell catalysts. Reprinted with permission from ref. 118. Copyright 2017 ACS.



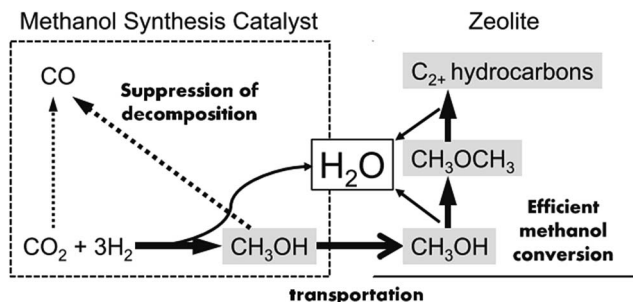


Fig. 11 Reaction steps of CO<sub>2</sub> hydrogenation over composite catalyst (favorable paths are shown in bold lines). Reprinted with permission from ref. 125. Copyright 2015 Elsevier.

There are some differences between CO<sub>2</sub> hydrogenation and CO hydrogenation to hydrocarbons through the methanol-mediated route, such as the molecular polarity,<sup>105</sup> number of C–O bonds and adsorption capacity of reactants.<sup>144</sup> However, there are also some similarities, such as the subsequent reaction on the zeolites when methanol is formed. So, the design of bifunctional catalysts for CO<sub>2</sub> hydrogenation can be inspired by the syngas conversion catalysts. Recently, the products of syngas conversion over the bifunctional catalysts have broken through the traditional ASF distribution and giving the desired products selectively. Wang *et al.*<sup>145,146</sup> prepared mesoporous H-ZSM-5-supported cobalt nanoparticles for conversion of syngas to hydrocarbons. The C<sub>5</sub>–C<sub>11</sub> selectivity can reach as high as *ca.* 70% which was due to the hydrocracking/isomerization of the higher hydrocarbons on the Brønsted acidic sites of H-ZSM-5. A series of core–shell catalysts (Fe–Zn–Zr@zeolites) were synthesized by Wang *et al.*<sup>124</sup> to adjust product distribution, especially in an attempt to improve isoalkane content by the confinement effect. Over 80% isoalkanes among all hydrocarbons were produced on Fe–Zn–Zr@HZSM5-Hbeta catalyst.

Wang and co-workers also integrated the methanol synthesis and methanol-to-olefins reactions with a bifunctional catalyst, Zr–Zn (2 : 1)/SAPO-34. The C<sub>2</sub>–C<sub>4</sub> olefin selectivity can reach 74% with a CO conversion of 11% at 673 K, thus breaking the limitation of ASF distribution.<sup>103</sup> Furthermore, Wang *et al.* synthesized ZnGa<sub>2</sub>O<sub>4</sub>/SAPO-34 for CO<sub>2</sub> hydrogenation to C<sub>2</sub>–C<sub>4</sub> olefins with a selectivity of 86% using the oxygen vacancies on ZnGa<sub>2</sub>O<sub>4</sub> to activate CO<sub>2</sub> molecules.<sup>121</sup> Additionally, the importance of oxygen vacancies was also evidenced by Sun and co-workers. They prepared a bifunctional catalyst composed of indium–zirconium composite oxide and SAPO-34 zeolite which offered C<sub>2</sub>–C<sub>4</sub> selectivity as high as 80% at more than 35% CO<sub>2</sub> conversion.<sup>123</sup> DFT calculations revealed that In<sub>2</sub>O<sub>3</sub> was a unique catalyst in CO<sub>2</sub> activation and hydrogenation to methanol with its surface oxygen vacancies and that the reaction followed a mechanism comprising the cyclic creation and annihilation of oxygen vacancies.<sup>147</sup> These results indicated that the incorporation of Zr into In<sub>2</sub>O<sub>3</sub> created new kinds of vacancies with high concentration, which progressively enhanced the reaction rate evidenced by DFT calculations. It is worth noting that no obvious deactivation is observed over 150 h, indicating a promising potential for industrial application. Bao *et al.*<sup>148</sup>

presented a process to eliminate the ASF distribution for synthesis gas to light olefins that was enabled by a bifunctional catalyst with two types of active sites. The partially reduced oxide surface (ZnCrO<sub>x</sub>) activated CO and H<sub>2</sub>, and C–C coupling was subsequently manipulated within the confined acidic pores of SAPO zeolites. They suggested that the appropriate distance of the two active sites was beneficial for C<sub>2</sub>–C<sub>4</sub> formation. The C<sub>2</sub>–C<sub>4</sub> selectivity could be optimized as high as 80%, and the C<sub>2</sub>–C<sub>4</sub> selectivity was 94%, which broke the theoretical limit of only 58% for C<sub>2</sub>–C<sub>4</sub> hydrocarbons as well. Li *et al.*<sup>122</sup> also fabricated a tandem catalyst, ZnZrO/SAPO-34, for CO<sub>2</sub> conversion with a selectivity for lower olefins as high as 80–90% among hydrocarbon products. It is proposed that CO<sub>2</sub> and H<sub>2</sub> were activated on ZnZrO and the C–C bond formation was performed on SAPO through DRIFT characterization. CH<sub>x</sub>O was considered as intermediate species that included not only methanol. This tandem catalyst showed a resistance to thermal and sulfur treatments (H<sub>2</sub>S and SO<sub>2</sub>), suggesting promising potential application in industry.

The current results have demonstrated that the preparation of bifunctional catalysts combining metal oxides and zeolites is an effective way to control product selectivity for C<sub>1</sub> conversion, and the appropriate hydrogenation ability of the two components in such bifunctional catalyst is crucial for adjusting product selectivity.

In summary, CO<sub>2</sub> hydrogenation to C<sub>2+</sub> hydrocarbons can be catalyzed through modified FTS route or methanol-mediated route to promote hydrocarbon chain growth. For the modified FTS metal-based catalysts, appropriate active metal should be chosen, such as Fe, to get the best hydrogenation capacity. The support basicity and oxygen vacancies should also be improved to increase CO<sub>2</sub> adsorption and activation.<sup>62</sup> In addition, adding promoters to adjust the surface C/H ratio and reduction capacity of the active metal is another approach to promote hydrocarbon chain growth.<sup>116,120,135</sup> For the methanol-mediated route, bifunctional catalysts combining metal oxides and zeolites are crucial for obtaining a higher selectivity of long-chain hydrocarbons. Acid sites are important for the conversion of methanol to hydrocarbons and the channel diameter can influence product selectivities due to the shape-selectivity characteristic.<sup>143</sup> SAPO-34 with 8-ring pore structure is beneficial for C<sub>2</sub>–C<sub>4</sub> formation<sup>148</sup> and ZSM-5 with 10-ring pore structure will lead to C<sub>5</sub>–C<sub>11</sub> formation.<sup>105</sup> Therefore, tuning acid strength and pore size plays a significant role in the formation of C<sub>2+</sub> hydrocarbons and it is a promising direction to promote chain growth.

### 3.3 Mechanisms of C–C coupling

There is an essential and very large difference between CO<sub>2</sub> methanation and CO<sub>2</sub> hydrogenation to C<sub>2+</sub> hydrocarbons, which is the C–C coupling barrier for C<sub>2+</sub> hydrocarbon formation. In light of the hydrocarbon formation mechanism, the key point for producing long-chain hydrocarbons is controlling the active H/C to an appropriate ratio, wherein too much surface H\* will lead to excessive hydrogenation and methane formation, while the opposite condition will offset the hydrogenation



ability and reduce the activity of CO<sub>2</sub> conversion. Satthawong and co-workers added different amounts of potassium to Fe–Co bimetallic catalysts to tune the product selectivity. The CO<sub>2</sub> adsorption was promoted and the H<sub>2</sub> adsorption was suppressed with increasing K content through CO<sub>2</sub>-TPD and H<sub>2</sub>-TPD; the C<sub>5+</sub> selectivity also increased with more potassium addition. However, when the K/Fe atomic ratio increased from 0.5 to 1, the CO<sub>2</sub> conversion decreased. They attributed the selectivity of the product to the type and concentration of chemisorbed hydrogen and carbon dioxide on the catalyst surface.<sup>116</sup> Apparently, tuning the surface H/C ratios to manipulate and optimize the product distribution appears to be decisive in the synthesis of C<sub>2+</sub> hydrocarbons *via* CO<sub>2</sub> hydrogenation.

The crucial step of hydrocarbon synthesis by CO<sub>2</sub> hydrogenation is first C–C bond formation and C–O bond cleavage. Many computational studies have been conducted to investigate the C–C coupling step over various catalysts.<sup>149–157</sup> Different metals showed diverse catalytic performances. Co- and Fe-based catalysts are widely used to catalyze CO<sub>2</sub> or CO hydrogenation to hydrocarbons.<sup>158–163</sup> Cu with unfavorable ability for C–O bond cleavage usually converted CO<sub>2</sub> or CO to C<sub>2+</sub> hydrocarbons<sup>164</sup> or alcohols.<sup>28,150,165–168</sup>

**3.3.1 C–C coupling over Fe-based catalysts.** Fe-based catalysts are widely used in FTS for hydrocarbon production. Due to the similarity, Fe becomes one of the most important components in the catalysts for CO<sub>2</sub> hydrogenation to hydrocarbons. Pham *et al.*<sup>155,157</sup> studied CO activation and hydrogenation over  $\chi$ -Fe<sub>5</sub>C<sub>2</sub>(510) surface, the most exposed one among the various facets due to its stability.<sup>157</sup> The carbon chain growth was more favorable than CH<sub>4</sub> formation due to the high barrier of CH<sub>2</sub><sup>\*</sup> and CH<sub>3</sub><sup>\*</sup> hydrogenation.<sup>155</sup> Compared with the CO<sup>\*</sup> insertion mechanism, CH<sub>x</sub><sup>\*</sup> coupling appeared to be a possible C<sub>2</sub> hydrocarbon synthesis route on the  $\chi$ -Fe<sub>5</sub>C<sub>2</sub>(510) surface. The chemisorbed CO<sup>\*</sup> dissociated to become C<sup>\*</sup> on the  $\chi$ -Fe<sub>5</sub>C<sub>2</sub>(510) surface, and was hydrogenated to CH<sup>\*</sup> species in the following step. C<sup>\*</sup> + CH<sup>\*</sup> and CH<sup>\*</sup> + CH<sup>\*</sup> were the most likely coupling pathways, and were characterized with carbide mechanism.

Recently Nie *et al.*<sup>109</sup> studied C–C coupling over Fe–Cu bimetallic catalysts (Fig. 12). CH<sup>\*</sup> was proposed as the most likely monomer over both pure Fe(100) and Cu-doped Fe(100) surfaces, though CH<sup>\*</sup> formation was quite different over the two surfaces. On the Fe(100) facet, CO<sub>2</sub> was directly dissociated to form CO<sup>\*</sup> then to CH<sup>\*</sup> through subsequent hydrogenation. Differently, the intermediate CO<sup>\*</sup> was transformed to HCOO<sup>\*</sup> then to CH<sup>\*</sup> through hydrogenation and dissociation in sequence on the Cu-doped Fe(100) facet. The pure Fe(100) favored CH<sub>4</sub> synthesis with a low barrier of CH<sup>\*</sup> hydrogenation, while Cu promoted C<sub>2</sub>H<sub>4</sub> synthesis with a low barrier CH<sup>\*</sup> + CH<sup>\*</sup>. The CH<sub>x</sub><sup>\*</sup> coupling pathway was also proposed as a plausible mechanism for C<sub>2</sub> hydrocarbon synthesis over other iron facets.<sup>169,170</sup> Clearly, the appropriate catalysts for CO<sub>2</sub> hydrogenation to hydrocarbons do not always go through the CO route (modified FTS route), which offers an alternative to break the restraint of the ASF distribution and the equilibrium conversion of CO<sub>2</sub> to methanol.

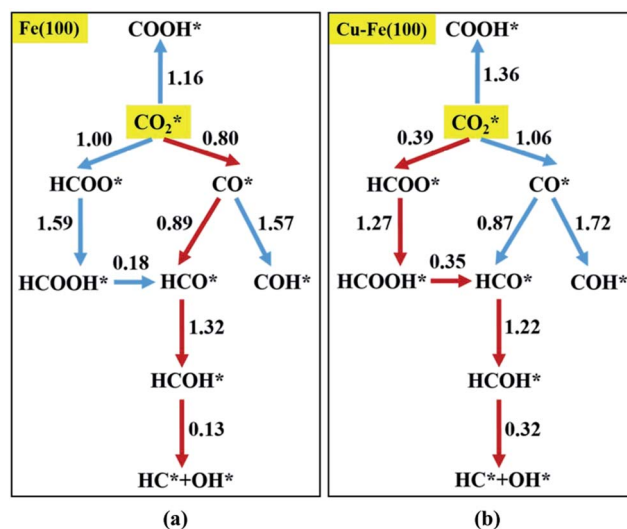


Fig. 12 Reaction networks examined to identify energetically favorable C1 species from CO<sub>2</sub> hydrogenation on (a) Fe(100) and (b) Cu–Fe(100) surface at 4/9 ML Cu coverage. Activation barriers are given in eV (the networks connected with red arrows represent the preferred path for CO<sub>2</sub> conversion to CH<sup>\*</sup>). Reprinted with permission from ref. 109. Copyright 2017 ACS.

**3.3.2 C–C coupling over Cu-based catalysts.** Cu-based catalysts are widely used for CO<sub>2</sub> hydrogenation. Ou *et al.*<sup>149,150</sup> attributed the initial C–C bond formation to CO<sup>\*</sup> dimerization on the Cu(100) facet. The product distribution varied depending on different facets of Cu during the CO<sub>2</sub> hydrogenation. C<sub>2</sub>H<sub>4</sub> was formed more favorably on the Cu(100) surface, and CH<sub>4</sub> was the main product on the Cu(111) surface under chemical conditions. CO was formed through both the direct dissociation of CO<sub>2</sub> over Cu(100) surface and the dissociative hydrogenation over Cu(111) surface. The CO<sup>\*</sup> dimerization was more favorable than CO<sup>\*</sup> hydrogenation to CHO<sup>\*</sup> in terms of kinetics. The CO<sup>\*</sup> dimer then underwent further hydrogenation to form C<sub>2</sub>H<sub>4</sub> on the Cu(100) surface as depicted in Fig. 13, while CO<sup>\*</sup> hydrogenation with CHO<sup>\*</sup> as the main intermediate produced CH<sub>4</sub>. Recently Xiao *et al.*<sup>151</sup> proposed a pH-dependent route for C<sub>1</sub> and C<sub>2</sub> product formation over Cu(111) facets. The preferred pathway for C<sub>2</sub>H<sub>4</sub> formation under aqueous condition was CO → COH → CO–COH → COH–COH → C–COH → C–HCOH → C–CH → C–CH<sub>2</sub> → CH–CH<sub>2</sub> → CH–CH<sub>3</sub> → CH<sub>2</sub>–CH<sub>3</sub> → CH<sub>2</sub>–CH<sub>2</sub>, which is similar to the CO<sup>\*</sup> dimerization mechanism on the Cu(100) surface.

Compared with the CO<sup>\*</sup> dimerization mechanism, CO<sup>\*</sup> coupled with CH<sub>x</sub><sup>\*</sup> also contributed to hydrocarbon formation over Cu-based catalysts. Wang *et al.*<sup>152–154</sup> investigated the effect of Cu on higher alcohol and hydrocarbon formation. The higher alcohol formation was facilitated by lowering the barrier of CO<sup>\*</sup> coupling with CH<sub>x</sub><sup>\*</sup> using copper as the promoter over Co-based catalysts.<sup>153</sup> The C<sub>2</sub> oxygenate was the main product over CuΣ5(310) surface by CO<sup>\*</sup> coupling with CH<sub>2</sub><sup>\*</sup> which could not occur over pure Cu(111) and Cu(100) facets.<sup>152</sup> The coverage of CH<sub>2</sub><sup>\*</sup> has an essential role in this mechanism. Cu exhibited much better catalytic performance for the association reaction than Co and Ni, while Co benefited the dissociation





Fig. 13 Proposed reduction pathways for the production of  $C_2H_4$  in the reduction mechanism of CO dimer on Cu(100). Reprinted with permission from ref. 150. Copyright 2015 RSC.

reaction.<sup>154,171</sup> With the assistance of Co and the Cu $\Sigma$ 5(310) surface's special active sites, the formation of  $CH_2^*$  was accelerated, and the  $CO^*$  coupling mechanism was favored. Co and Ni were capable of catalyzing CO to  $CH^*$  and further to  $CH_2^*$  as the favorable monomer. Due to the low barrier of  $CO^*$  insertion into  $CH_2^*$  over Co(111), the Co-based catalysts favored chain growth. On the other hand, Ni-based catalysts were used for CO or  $CO_2$  methanation with higher barrier of  $CO^*$  insertion and lower barrier of  $CH_x^*$  hydrogenation.<sup>92,154,172,173</sup> Zhang *et al.*<sup>171</sup> investigated the CO hydrogenation over Co-decorated Cu alloy catalyst, and stated that the Co-Cu(211) surface was conducive to ethanol formation rather than methane or methanol, and the C-C coupling was accomplished by interacting  $CO^*$  with  $CH_2^*$  and  $CH_3^*$ .

Zuo *et al.*<sup>156</sup> explored ethanol synthesis by syngas over alloy-like CoCu(111) surface, and they found that  $CO^* + CH_3^*$  was the most likely pathway of coupling. The above computational studies demonstrate that  $CO^*$ , as the main intermediate or the reactant during  $CO_2$  hydrogenation, was able to interact with surface  $CO^*$  or  $CH_x^*$  species over Cu- and Co-based catalysts, through which C-C coupling was available for the formation of long-chain products.

### 3.4 Deactivation of catalysts for $CO_2$ hydrogenation to hydrocarbons

Lee *et al.*<sup>174</sup> investigated the reasons for deactivation of Fe-K/ $\gamma$ - $Al_2O_3$  for  $CO_2$  hydrogenation to hydrocarbons through XPS,

HR-TEM, TPO, and Mössbauer spectroscopy. The reasons for deactivation are different at different positions in the reactor. As time progressed, the  $Fe_2O_3$  was reduced to active phase  $\chi$ - $Fe_5C_3$  and finally the  $\chi$ - $Fe_5C_3$  was transformed to  $\theta$ - $FeC_3$ , which is not an active species for  $CO_2$  hydrogenation. Hence, in the inlet reactor region, the deactivation pathway was phase transformation. Conversely, the main factor at the outlet part of the reactor was coke deposition.

Li *et al.*<sup>117</sup> observed the remarkable metal sintering on supported FeCo/ZrO<sub>2</sub> catalysts which was responsible for the rapid deactivation of activity. In contrast, Fe-Co-Zr polymetallic fibers obtained by a one-step electrospinning technique showed stable activity over the reaction period. Co and Fe were dispersed in proximity to ZrO<sub>2</sub>, but separately from each other, which, in turn, helped reduce the possibility of sintering. Active metals encapsulated in hollow zeolite<sup>175</sup> or confined in nanotubes<sup>176</sup> were also applied to resist metal sintering and increase catalyst stability, which are good references for  $CO_2$  hydrogenation catalysts.

## 4. Conclusion and prospects

Environmental issues have pushed the necessity to reduce  $CO_2$  emissions caused by the use of fossil fuels. Many efforts have been made to develop catalysts and understand the reaction mechanisms. Heterogeneous thermocatalysis is a promising direction for application in  $CO_2$  conversion. The catalyst performance can be affected by many factors, such as metal-support interaction,



metal particle size and promoters. Ni-based catalysts are mainly used in CH<sub>4</sub> production from CO<sub>2</sub> hydrogenation. In addition, Co, Ru, Ir and Rh are also applied for CO<sub>2</sub> methanation. Fe is an active metal for CO<sub>2</sub> hydrogenation to C<sub>2+</sub> hydrocarbons through modified FTS route or methanol-mediated route. Fe–metal bimetallic catalysts have shown markedly improved performance. The preparation of bifunctional catalysts combining metal oxides and zeolites is an effective way to control the product selectivity for C1 conversion. Some experiments and DFT calculations have given the encouraging result that CO<sub>2</sub> conversion can be catalyzed through the formate intermediate route which is neither the CO route nor the methanol route, which will not be limited by the ASF distribution and the equilibrium conversion of CO<sub>2</sub> to methanol. The crucial mechanisms of the initial C–C bond formation and C–O bond cleavage are different between Fe-based catalysts and Cu-based catalysts in DFT calculations.

In general, future research directions for CO<sub>2</sub> hydrogenation are proposed as follows:

1. To adjust the catalyst surface H/C ratio and facilitate C–C coupling and generate high-value-added products.
2. To improve the support basicity and oxygen vacancies and increase the CO<sub>2</sub> adsorption and activation.
3. To explore more novel catalytic materials and improve the catalyst stability.
4. To explore more active catalysts for low-temperature and energy-saving CO<sub>2</sub> hydrogenation.

## Conflicts of interest

There are no conflicts to declare.

## Acknowledgements

This work was financially supported by the National Key Research and Development Program of China (2016YFB0600902-5).

## References

- 1 B. Kahn, *Earth's CO<sub>2</sub> Passes the 400 PPM Threshold—Maybe Permanently*, Climate Central, 2016.
- 2 *A Roadmap for moving to a competitive low carbon economy in 2050*, European Commission, 2011.
- 3 T. Sakakura, J. C. Choi and H. Yasuda, *Chem. Rev.*, 2007, **107**, 2365–2387.
- 4 I. Dimitriou, P. García-Gutiérrez, R. H. Elder, R. M. Cuéllar-Franca, A. Azapagic and R. W. K. Allen, *Energy Environ. Sci.*, 2015, **8**, 1775–1789.
- 5 X. Ma, X. Wang and C. Song, *J. Am. Chem. Soc.*, 2009, **131**, 5777–5783.
- 6 P. J. Lunde and F. L. Kester, *Ind. Eng. Chem. Process Des. Dev.*, 1974, **13**, 27–33.
- 7 G. Du, S. Lim, Y. Yang, C. Wang, L. Pfefferle and G. L. Haller, *J. Catal.*, 2007, **249**, 370–379.
- 8 M. S. Duyar, M. A. A. Treviño and R. J. Farrauto, *Appl. Catal., B*, 2015, **168–169**, 370–376.
- 9 Y. Yoon, A. S. Hall and Y. Surendranath, *Angew. Chem., Int. Ed.*, 2016, **128**, 1–6.
- 10 K. Li, B. Peng and T. Peng, *ACS Catal.*, 2016, **6**, 7485–7527.
- 11 P. G. Jessop, F. Joó and C. C. Tai, *Coord. Chem. Rev.*, 2004, **248**, 2425–2442.
- 12 W. Wang, S. Wang, X. Ma and J. Gong, *Chem. Soc. Rev.*, 2011, **40**, 3703–3727.
- 13 J. Ma, N. Sun, X. Zhang, N. Zhao, F. Xiao, W. Wei and Y. Sun, *Catal. Today*, 2009, **148**, 221–231.
- 14 S. Saeidi, N. A. S. Amin and M. R. Rahimpour, *J. CO<sub>2</sub> Util.*, 2014, **5**, 66–81.
- 15 G. Centi and S. Perathoner, *Catal. Today*, 2009, **148**, 191–205.
- 16 G. Centi and S. Perathoner, *Greenhouse Gases: Sci. Technol.*, 2011, **1**, 21–35.
- 17 L. Zhou, Q. Wang, L. Ma, J. Chen, J. Ma and Z. Zi, *Catal. Lett.*, 2015, **145**, 612–619.
- 18 A. Westermann, B. Azambre, M. C. Bacariza, I. Graca, M. F. Ribeiro, J. M. Lopes and C. Henriques, *Appl. Catal., B*, 2015, **174**, 120–125.
- 19 D. C. Upham, A. R. Derk, S. Sharma, H. Metiu and E. W. McFarland, *Catal. Sci. Technol.*, 2015, **5**, 1783–1791.
- 20 N. Shimoda, D. Shoji, K. Tani, M. Fujiwara, K. Urasaki, R. Kikuchi and S. Satokawa, *Appl. Catal., B*, 2015, **174**, 486–495.
- 21 R. Razaq, C. Li, M. Usman, K. Suzuki and S. Zhang, *Chem. Eng. J.*, 2015, **262**, 1090–1098.
- 22 S. K. Beaumont, S. Alayoglu, C. Specht, W. D. Michalak, V. V. Pushkarev, J. Guo, N. Kruse and G. A. Somorjai, *J. Am. Chem. Soc.*, 2014, **136**, 9898–9901.
- 23 F. Wang, C. Li, X. Zhang, M. Wei, D. G. Evans and X. Duan, *J. Catal.*, 2015, **329**, 177–186.
- 24 M. D. Porosoff, B. Yan and J. G. Chen, *Energy Environ. Sci.*, 2016, **9**, 62–73.
- 25 C. G. Visconti, M. Martinelli, L. Falbo, A. Infantes-Molina, L. Lietti, P. Forzatti, G. Iaquaniello, E. Palo, B. Picutti and F. Brignoli, *Appl. Catal., B*, 2017, **200**, 530–542.
- 26 P. Gao, S. Li, X. Bu, S. Dang, Z. Liu, H. Wang, L. Zhong, M. Qiu, C. Yang, J. Cai, W. Wei and Y. Sun, *Nat. Chem.*, 2017, **9**, 1019–1024.
- 27 H. Song, N. Zhang, C. Zhong, Z. Liu, M. Xiao and H. Gai, *New J. Chem.*, 2017, **41**, 9170–9177.
- 28 K. Larmier, W. C. Liao, S. Tada, E. Lam, R. Verel, A. Bansode, A. Urakawa, A. Comas-Vives and C. Coperet, *Angew. Chem., Int. Ed.*, 2017, **56**, 1–7.
- 29 X. Jiang, N. Koizumi, X. Guo and C. Song, *Appl. Catal., B*, 2015, **170–171**, 173–185.
- 30 S. Bai, Q. Shao, P. Wang, Q. Dai, X. Wang and X. Huang, *J. Am. Chem. Soc.*, 2017, **139**, 6827–6830.
- 31 K. Mazloomi, N. Sulaiman and H. Moayed, *Int. J. Electrochem. Sci.*, 2012, **7**, 3314–3326.
- 32 M. S. Duyar, A. Ramachandran, C. Wang and R. J. Farrauto, *J. CO<sub>2</sub> Util.*, 2015, **12**, 27–33.
- 33 B. Mutz, H. W. P. Carvalho, S. Mangold, W. Kleist and J. D. Grunwaldt, *J. Catal.*, 2015, **327**, 48–53.





- 34 M. Younas, L. L. Kong, M. J. K. Bashir, H. Nadeem, A. Shehzad and S. Sethupathi, *Energy Fuels*, 2016, **30**, 8815–8831.
- 35 S. Rönsch, J. Schneider, S. Matthischke, M. Schlüter, M. Götz, J. Lefebvre, P. Prabhakaran and S. Bajohr, *Fuel*, 2016, **166**, 276–296.
- 36 M. Y. K. Hashimoto and S. Meguro, *Corros. Sci.*, 2002, **44**, 371–386.
- 37 A. D. Tomsett, T. Haginwara, A. Miyamoto and T. Inui, *Appl. Catal.*, 1986, **26**, 391.
- 38 K. R. Thampi, J. Kiwi and M. Gratzel, *Nature*, 1987, **327**, 506.
- 39 J. Gao, Y. Wang, Y. Ping, D. Hu, G. Xu, F. Gu and F. Su, *RSC Adv.*, 2012, **2**, 2358.
- 40 F. Koschany, D. Schlereth and O. Hinrichsen, *Appl. Catal., B*, 2016, **181**, 504–516.
- 41 J. Janlamool, P. Praserttham and B. Jongsomjit, *J. Nat. Gas Chem.*, 2011, **20**, 558–564.
- 42 Z. Guillin, W. Tian, X. Hongmei and Z. Xuxu, *Int. J. Hydrogen Energy*, 2013, **38**, 10012–10018.
- 43 G. L. Zhou, T. Wu, H. B. Zhang, H. M. Xie and Y. C. Feng, *Chem. Eng. Commun.*, 2014, **201**, 233–240.
- 44 H. H. Shin, L. Lu, Z. Yang, C. J. Kiely and S. McIntosh, *ACS Catal.*, 2016, **6**, 2811–2818.
- 45 I. Rossetti, C. Biffi, C. L. Bianchi, V. Nichele, M. Signoretto, F. Menegazzo, E. Finocchio, G. Ramis and A. Di Michele, *Appl. Catal., B*, 2012, **117–118**, 384–396.
- 46 D. Theleritis, S. Souentie, A. Siokou, A. Katsaounis and C. G. Vayenas, *ACS Catal.*, 2012, **2**, 770–780.
- 47 J. H. Kwak, L. Kovarik and J. Szanyi, *ACS Catal.*, 2013, **3**, 2449–2455.
- 48 A. Karelovic and P. Ruiz, *Appl. Catal., B*, 2012, **113–114**, 237–249.
- 49 J. N. Park and E. W. McFarland, *J. Catal.*, 2009, **266**, 92–97.
- 50 J. H. Kwak, L. Kovarik and J. Szanyi, *ACS Catal.*, 2013, **3**, 2094–2100.
- 51 J. Liu, D. Cui, J. Yu, F. Su and G. Xu, *Chin. J. Chem. Eng.*, 2015, **23**, 86–92.
- 52 M. A. A. Aziz, A. A. Jalil, S. Triwahyono, R. R. Mukti, Y. H. Taufiq-Yap and M. R. Sazegar, *Appl. Catal., B*, 2014, **147**, 359–368.
- 53 Z. Q. Wang, Z. N. Xu, S. Y. Peng, M. J. Zhang, G. Lu, Q. S. Chen, Y. Chen and G. C. Guo, *ACS Catal.*, 2015, **5**, 4255–4259.
- 54 G. R. Johnson and A. T. Bell, *ACS Catal.*, 2016, **6**, 100–114.
- 55 G. Zeng, J. Qiu, Z. Li, P. Pavaskar and S. B. Cronin, *ACS Catal.*, 2014, **4**, 3512–3516.
- 56 S. Kattel, W. Yu, X. Yang, B. Yan, Y. Huang, W. Wan, P. Liu and J. G. Chen, *Angew. Chem., Int. Ed.*, 2016, **55**, 1–7.
- 57 Y. Liu, K. Fang, J. Chen and Y. Sun, *Green Chem.*, 2007, **9**, 611.
- 58 S. Sokolov, E. V. Kondratenko, M. M. Pohl, A. Barkschat and U. Rodemerck, *Appl. Catal., B*, 2012, **113–114**, 19–30.
- 59 V. Nichele, M. Signoretto, F. Menegazzo, A. Gallo, V. Dal Santo, G. Cruciani and G. Cerrato, *Appl. Catal., B*, 2012, **111–112**, 225–232.
- 60 A. M. Abdel-Mageed, D. Widmann, S. E. Olesen, I. Chorkendorff, J. Biskupek and R. J. Behm, *ACS Catal.*, 2015, **5**, 6753–6763.
- 61 S. Kattel, P. Liu and J. Chen, *J. Am. Chem. Soc.*, 2017, **139**, 9739–9754.
- 62 W. Li, X. Nie, X. Jiang, A. Zhang, F. Ding, M. Liu, Z. Liu, X. Guo and C. Song, *Appl. Catal., B*, 2018, **220**, 397–408.
- 63 G. Zhou, H. Liu, K. Cui, H. Xie, Z. Jiao, G. Zhang, K. Xiong and X. Zheng, *Int. J. Hydrogen Energy*, 2017, **42**, 16108–16117.
- 64 G. Zhou, H. Liu, K. Cui, A. Jia, G. Hu, Z. Jiao, Y. Liu and X. Zhang, *Appl. Surf. Sci.*, 2016, **383**, 248–252.
- 65 N. M. Martin, P. Velin, M. Skoglundh, M. Bauer and P. A. Carlsson, *Catal. Sci. Technol.*, 2017, **7**, 1086–1094.
- 66 J. A. H. Dreyer, P. Li, L. Zhang, G. K. Beh, R. Zhang, P. H. L. Sit and W. Y. Teoh, *Appl. Catal., B*, 2017, **219**, 715–726.
- 67 A. Kim, C. Sanchez, G. Patriarche, O. Ersen, S. Moldovan, A. Wisnet, C. Sassoie and D. P. Debecker, *Catal. Sci. Technol.*, 2016, **6**, 8117–8128.
- 68 A. Kim, D. P. Debecker, F. Devred, V. Dubois, C. Sanchez and C. Sassoie, *Appl. Catal., B*, 2018, **220**, 615–625.
- 69 Y. Lin, Y. Zhu, X. Pan and X. Bao, *Catal. Sci. Technol.*, 2017, **7**, 2813–2818.
- 70 H. C. Wu, Y. C. Chang, J. H. Wu, J. H. Lin, I. K. Lin and C. S. Chen, *Catal. Sci. Technol.*, 2015, **5**, 4154–4163.
- 71 V. Iablokov, S. K. Beaumont, S. Alayoglu, V. V. Pushkarev, C. Specht, J. Gao, A. P. Alivisatos, N. Kruse and G. A. Somorjai, *Nano Lett.*, 2012, **12**, 3091–3096.
- 72 J. C. Matsubu, V. N. Yang and P. Christopher, *J. Am. Chem. Soc.*, 2015, **137**, 3076–3084.
- 73 S. Li, Y. Xu, Y. Chen, W. Li, L. Lin, M. Li, Y. Deng, X. Wang, B. Ge, C. Yang, S. Yao, J. Xie, Y. Li, X. Liu and D. Ma, *Angew. Chem., Int. Ed.*, 2017, **56**, 1–6.
- 74 Y. Yan, Y. Dai, H. He, Y. Yu and Y. Yang, *Appl. Catal., B*, 2016, **196**, 108–116.
- 75 D. Wierzbicki, R. Debek, M. Motak, T. Grzybek, M. E. Gálvez and P. Da Costa, *Catal. Commun.*, 2016, **83**, 5–8.
- 76 L. Xu, F. Wang, M. Chen, D. Nie, X. Lian, Z. Lu, H. Chen, K. Zhang and P. Ge, *Int. J. Hydrogen Energy*, 2017, **42**, 15523–15539.
- 77 M. P. Andersson, F. Abild-Pedersen, I. N. Remediakis, T. Bligaard, G. Jones, J. Engbæk, O. Lytken, S. Horch, J. H. Nielsen, J. Sehested, J. R. Rostrup-Nielsen, J. K. Nørskov and I. Chorkendorff, *J. Catal.*, 2008, **255**, 6–19.
- 78 H. Wang, K. Xu, X. Yao, D. Ye, T. Pei, H. Hu, M. Qiao, Z. H. Li, X. Zhang and B. Zong, *ACS Catal.*, 2018, **8**, 1207–1211.
- 79 S. Abate, C. Mebrahtu, E. Giglio, F. Deorsola, S. Bensaid, S. Perathoner, R. Pirone and G. Centi, *Ind. Eng. Chem. Res.*, 2016, **55**, 4451–4460.
- 80 S. Abate, K. Barbera, E. Giglio, F. Deorsola, S. Bensaid, S. Perathoner, R. Pirone and G. Centi, *Ind. Eng. Chem. Res.*, 2016, **55**, 8299–8308.



- 81 T. Kajiwara, M. Higuchi, D. Watanabe, H. Higashimura, T. Yamada and H. Kitagawa, *Chem.–Eur. J.*, 2014, **20**, 15611–15617.
- 82 O. M. Yaghi, M. O’Keeffe, N. W. Ockwig, H. K. Chae, M. Eddaoudi and J. Kim, *Nature*, 2003, **423**, 705–714.
- 83 B. Chen, S. Xiang and G. Qian, *Acc. Chem. Res.*, 2010, **43**, 1115–1124.
- 84 W. Zhen, B. Li, G. Lu and J. Ma, *Chem. Commun.*, 2015, **51**, 1728–1731.
- 85 W. Li, A. Zhang, X. Jiang, C. Chen, Z. Liu, C. Song and X. Guo, *ACS Sustainable Chem. Eng.*, 2017, **5**, 7824–7831.
- 86 N. Srisawad, W. Chaitree, O. Mekasuwandumrong, A. Shotipruk, B. Jongsomjit and J. Panpranot, *React. Kinet., Mech. Catal.*, 2012, **107**, 179–188.
- 87 G. Zhan and H. C. Zeng, *ACS Catal.*, 2017, **7**, 7509–7519.
- 88 J. Ashok, M. L. Ang and S. Kawi, *Catal. Today*, 2017, **281**, 304–311.
- 89 M. Schubert, S. Pokhrel, A. Thomé, V. Zielasek, T. M. Gesing, F. Roessner, L. Mädler and M. Bäumer, *Catal. Sci. Technol.*, 2016, **6**, 7449–7460.
- 90 S. Danaci, L. Protasova, J. Lefevre, L. Bedel, R. Guilet and P. Marty, *Catal. Today*, 2016, **273**, 234–243.
- 91 R. Zhou, N. Rui, Z. Fan and C. J. Liu, *Int. J. Hydrogen Energy*, 2016, **41**, 22017–22025.
- 92 J. Ren, H. Guo, J. Yang, Z. Qin, J. Lin and Z. Li, *Appl. Surf. Sci.*, 2015, **351**, 504–516.
- 93 Q. Zheng, R. Farrauto and A. Chau Nguyen, *Ind. Eng. Chem. Res.*, 2016, **55**, 6768–6776.
- 94 Y. Li, G. Lu and J. Ma, *RSC Adv.*, 2014, **4**, 17420.
- 95 I. Graça, L. V. González, M. C. Bacariza, A. Fernandes, C. Henriques, J. M. Lopes and M. F. Ribeiro, *Appl. Catal., B*, 2014, **147**, 101–110.
- 96 F. Wang, S. He, H. Chen, B. Wang, L. Zheng, M. Wei, D. G. Evans and X. Duan, *J. Am. Chem. Soc.*, 2016, **138**, 6298–6305.
- 97 S. Sharma, K. B. Sravan Kumar, Y. M. Chandnani, V. S. Phani Kumar, B. P. Gangwar, A. Singhal and P. A. Deshpande, *J. Phys. Chem. C*, 2016, **120**, 14101–14112.
- 98 C. Heine, B. A. Lechner, H. Bluhm and M. Salmeron, *J. Am. Chem. Soc.*, 2016, **138**, 13246–13252.
- 99 A. Solis-Garcia, J. F. Louvier-Hernandez, A. Almendarez-Camarillo and J. C. Fierro-Gonzalez, *Appl. Catal., B*, 2017, **218**, 611–620.
- 100 J. K. Kesavana, I. Luisetto, S. Tuti, C. Meneghini, G. Iucci, C. Battocchio, S. Mobilio, S. Casciardi and R. Sisto, *J. CO<sub>2</sub> Util.*, 2018, **23**, 200–211.
- 101 H. Li, J. Ren, X. Qin, Z. Qin, J. Lin and Z. Li, *RSC Adv.*, 2015, **5**, 96504–96517.
- 102 A. A. Muleja, Y. Yao, D. Glasser and D. Hildebrandt, *Ind. Eng. Chem. Res.*, 2017, **56**, 469–478.
- 103 K. Cheng, B. Gu, X. Liu, J. Kang, Q. Zhang and Y. Wang, *Angew. Chem., Int. Ed.*, 2016, **55**, 4725–4728.
- 104 Y. Zheng, W. Zhang, Y. Li, J. Chen, B. Yu, J. Wang, L. Zhang and J. Zhang, *Nano Energy*, 2017, **40**, 512–539.
- 105 J. Wei, Q. Ge, R. Yao, Z. Wen, C. Fang, L. Guo, H. Xu and J. Sun, *Nat. Commun.*, 2017, **8**, 15174.
- 106 G. Pekridis, K. Kalimeri, N. Kaklidis, E. Vakouftsi, E. F. Iliopoulou, C. Athanasiou and G. E. Marnellos, *Catal. Today*, 2007, **127**, 337–346.
- 107 P. Kangvansura, L. M. Chew, W. Saengsui, P. Santawaja, Y. Poo-arporn, M. Muhler, H. Schulz and A. Worayingyong, *Catal. Today*, 2016, **275**, 59–65.
- 108 L. M. Chew, P. Kangvansura, H. Ruland, H. J. Schulte, C. Somsen, W. Xia, G. Eggeler, A. Worayingyong and M. Muhler, *Appl. Catal., A*, 2014, **482**, 163–170.
- 109 X. Nie, H. Wang, M. J. Janik, Y. Chen, X. Guo and C. Song, *J. Phys. Chem. C*, 2017, **121**, 13164–13174.
- 110 D. J. Dwyer and G. A. Somorjai, *J. Catal.*, 1978, **52**, 291–301.
- 111 H. D. Willauer, R. Ananth, M. T. Olsen, D. M. Drab, D. R. Hardy and F. W. Williams, *J. CO<sub>2</sub> Util.*, 2013, **3–4**, 56–64.
- 112 M. Albrecht, U. Rodemerck, M. Schneider, M. Bröring, D. Baabe and E. V. Kondratenko, *Appl. Catal., B*, 2017, **204**, 119–126.
- 113 G. B. Yu, B. Sun, Y. Pei, S. Xie, S. Yan, M. Qiao, K. Fan, X. Zhang and B. Zong, *J. Am. Chem. Soc.*, 2010, **132**, 935–937.
- 114 F. C. Emiel de Smit, A. M. Beale, O. V. Safonova, P. S. Wouter van Beek and B. M. Weckhuysen, *J. Am. Chem. Soc.*, 2010, **132**, 14928–14941.
- 115 L. Torrente-Murciano, R. S. Chapman, A. Narvaez-Dinamarca, D. Mattia and M. D. Jones, *Phys. Chem. Chem. Phys.*, 2016, **18**, 15496–15500.
- 116 R. Sathawong, N. Koizumi, C. Song and P. Prasassarakich, *Catal. Today*, 2015, **251**, 34–40.
- 117 W. Li, A. Zhang, X. Jiang, M. J. Janik, J. Qiu, Z. Liu, X. Guo and C. Song, *J. CO<sub>2</sub> Util.*, 2018, **23**, 219–225.
- 118 C. Xie, C. Chen, Y. Yu, J. Su, Y. Li, G. A. Somorjai and P. Yang, *Nano Lett.*, 2017, **17**, 3798–3802.
- 119 Y. H. Choi, Y. J. Jang, H. Park, W. Y. Kim, Y. H. Lee, S. H. Choi and J. S. Lee, *Appl. Catal., B*, 2017, **202**, 605–610.
- 120 M. Al-Dossary, A. A. Ismail, J. L. G. Fierro, H. Bouzid and S. A. Al-Sayari, *Appl. Catal., B*, 2015, **165**, 651–660.
- 121 X. Liu, M. Wang, C. Zhou, W. Zhou, K. Cheng, J. Kang, Q. Zhang, W. Deng and Y. Wang, *Chem. Commun.*, 2018, **54**, 140–143.
- 122 Z. Li, J. Wang, Y. Qu, H. Liu, C. Tang, S. Miao, Z. Feng, H. An and C. Li, *ACS Catal.*, 2017, **7**, 8544–8548.
- 123 P. Gao, S. Dang, S. Li, X. Bu, Z. Liu, M. Qiu, C. Yang, H. Wang, L. Zhong, Y. Han, Q. Liu, W. Wei and Y. Sun, *ACS Catal.*, 2017, **8**, 571–578.
- 124 X. Wang, G. Yang, J. Zhang, S. Chen, Y. Wu, Q. Zhang, J. Wang, Y. Han and Y. Tan, *Chem. Commun.*, 2016, **52**, 7352–7355.
- 125 M. Fujiwara, T. Satake, K. Shiokawa and H. Sakurai, *Appl. Catal., B*, 2015, **179**, 37–43.
- 126 M. Behrens, F. Studt, I. Kasatkin, S. Köhl, M. Hävecker, F. Abild-Pedersen, S. Zander, F. Girgsdies, P. Kurr, B. Knief, M. Tovar, R. Fischer, J. Nørskov and R. Schlögl, *Science*, 2012, **336**, 893–897.
- 127 F. Ding, A. Zhang, M. Liu, Y. Zuo, K. Li, X. Guo and C. Song, *Ind. Eng. Chem. Res.*, 2014, **53**, 17563–17569.
- 128 K. Zhao, W. Wang and Z. Li, *J. CO<sub>2</sub> Util.*, 2016, **16**, 236–244.



- 129 J. Wang, Z. You, Q. Zhang, W. Deng and Y. Wang, *Catal. Today*, 2013, **215**, 186–193.
- 130 X. Liu, Y. Jia, Y. Zhang, G. Ren, R. Feng, S. Zhang, M. Zaworotko and X. Bu, *Inorg. Chem. Front.*, 2016, **3**, 1510–1515.
- 131 B. Mousavi, S. Chaemchuen, B. Moosavi, Z. Luo, N. Gholampour and F. Verpoort, *New J. Chem.*, 2016, **40**, 5170–5176.
- 132 J. Ye and J. Johnson, *ACS Catal.*, 2015, **5**, 2921–2928.
- 133 S. Hu, M. Liu, F. Ding, C. Song, G. Zhang and X. Guo, *J. CO<sub>2</sub> Util.*, 2016, **15**, 89–95.
- 134 J. Wei, J. Sun, Z. Wen, C. Fang, Q. Ge and H. Xu, *Catal. Sci. Technol.*, 2016, **6**, 4786–4793.
- 135 T. Riedel, M. Claeys, H. Schulz, G. Schaub, S. Nam, K. Jun, M. Choi, G. Kishan and K. Lee, *Appl. Catal., A*, 1999, **186**, 201–213.
- 136 C. G. Visconti, M. Martinelli, L. Falbo, L. Fratolocchi and L. Lietti, *Catal. Today*, 2016, **277**, 161–170.
- 137 R. Sathawong, N. Koizumi, C. Song and P. Prasassarakich, *Top. Catal.*, 2014, **57**, 588–594.
- 138 R. Sathawong, N. Koizumi, C. Song and P. Prasassarakich, *J. CO<sub>2</sub> Util.*, 2013, **3–4**, 102–106.
- 139 Q. Zhang, J. Kang and Y. Wang, *ChemCatChem*, 2010, **2**, 1030–1058.
- 140 U. Rodemerck, M. Holeňá, E. Wagner, Q. Smejkal, A. Barkschat and M. Baerns, *ChemCatChem*, 2013, **5**, 1948–1955.
- 141 R. W. Dorner, D. R. Hardy, F. W. Williams and H. D. Willauer, *Energy Environ. Sci.*, 2010, **3**, 884.
- 142 O. Martin, A. J. Martín, C. Mondelli, S. Mitchell, T. F. Segawa, R. Hauert, C. Drouilly, D. Curulla-Ferré and J. Pérez-Ramírez, *Angew. Chem., Int. Ed.*, 2016, **55**, 6261–6265.
- 143 M. Fujiwara, H. Sakurai, K. Shiokawa and Y. Iizuka, *Catal. Today*, 2015, **242**, 255–260.
- 144 M. Kogler, E. M. Köck, B. Klötzer, L. Perfler and S. Penner, *J. Phys. Chem. C*, 2016, **120**, 3882–3898.
- 145 K. Cheng, L. Zhang, J. Kang, X. Peng, Q. Zhang and Y. Wang, *Chem.–Eur. J.*, 2015, **21**, 1928–1937.
- 146 J. Kang, K. Cheng, L. Zhang, Q. Zhang, J. Ding, W. Hua, Y. Lou, Q. Zhai and Y. Wang, *Angew. Chem., Int. Ed.*, 2011, **50**, 5200–5203.
- 147 J. Ye, C. Liu, D. Mei and Q. Ge, *ACS Catal.*, 2013, **3**, 1296–1306.
- 148 F. Jiao, J. Li, X. Pan, J. Xiao, H. Li, H. Ma, M. Wei, Y. Pan, Z. Zhou, M. Li, S. Miao, J. Li, Y. Zhu, D. Xiao, T. He, J. Yang, F. Qi, Q. Fu and X. Bao, *Science*, 2016, **351**, 1065–1068.
- 149 L. Ou, *J. Mol. Model.*, 2016, **22**, 246.
- 150 L. Ou, W. Long, Y. Chen and J. Jin, *RSC Adv.*, 2015, **5**, 96281–96289.
- 151 H. Xiao, T. Cheng and W. A. Goddard, *J. Am. Chem. Soc.*, 2017, **139**, 130–136.
- 152 J. Wang, Q. Sun, S. Chan and H. Su, *Appl. Catal., A*, 2016, **509**, 97–104.
- 153 J. Wang, X. Zhang, Q. Sun, S. Chan and H. Su, *Catal. Commun.*, 2015, **61**, 57–61.
- 154 J. Wang, Y. Kawazoe, Q. Sun, S. Chan and H. Su, *Surf. Sci.*, 2016, **645**, 30–40.
- 155 T. H. Pham, Y. Qi, J. Yang, X. Duan, G. Qian, X. Zhou, D. Chen and W. Yuan, *ACS Catal.*, 2015, **5**, 2203–2208.
- 156 Z. J. Zuo, F. Peng and W. Huang, *Sci. Rep.*, 2016, **6**, 34670.
- 157 T. H. Pham, X. Duan, G. Qian, X. Zhou and D. Chen, *J. Phys. Chem. C*, 2014, **118**, 10170–10176.
- 158 M. K. Gnanamani, G. Jacobs, H. H. Hamdeh, W. D. Shafer, F. Liu, S. D. Hopps, G. A. Thomas and B. H. Davis, *ACS Catal.*, 2016, **6**, 913–927.
- 159 A. Y. Khodakov, W. Chu and P. Fongarland, *Chem. Rev.*, 2007, **107**, 1692–1744.
- 160 M. D. Porosoff, B. Yan and J. G. Chen, *Energy Environ. Sci.*, 2016, **9**, 62–73.
- 161 P. Helden, J. Berg, M. Petersen, W. Rensburg, I. Ciobica and J. van de Loosdrecht, *Faraday Discuss.*, 2017, **197**, 117–151.
- 162 D. Chakrabarti, A. de Klerk, V. Prasad, M. Gnanamani, W. Shafer, G. Jacobs, D. Sparks and B. Davis, *Ind. Eng. Chem. Res.*, 2015, **54**, 1189–1196.
- 163 M. Landau, N. Meiri, N. Utsis, R. Vidruk Nehemya and M. Herskowitz, *Ind. Eng. Chem. Res.*, 2017, **56**, 13334–13355.
- 164 M. Bersani, K. Gupta, A. K. Mishra, R. Lanza, S. F. R. Taylor, H. U. Islam, N. Hollingsworth, C. Hardacre, N. H. de Leeuw and J. A. Darr, *ACS Catal.*, 2016, **6**, 5823–5833.
- 165 S. Kattel, B. Yan, Y. Yang, J. Chen and P. Liu, *J. Am. Chem. Soc.*, 2016, **138**, 12440–12450.
- 166 X. Nie, M. R. Esopi, M. J. Janik and A. Asthagiri, *Angew. Chem., Int. Ed.*, 2013, **52**, 2459–2462.
- 167 X. Nie, W. Luo, M. J. Janik and A. Asthagiri, *J. Catal.*, 2014, **312**, 108–122.
- 168 W. Luo, X. Nie, M. J. Janik and A. Asthagiri, *ACS Catal.*, 2016, **6**, 219–229.
- 169 H. J. Li, C. C. Chang and J. J. Ho, *J. Phys. Chem. C*, 2011, **115**, 11045–11055.
- 170 J. Cheng, P. Hu, P. Ellis, S. French, G. Kelly and C. M. Lok, *J. Phys. Chem. C*, 2008, **112**, 6082–6086.
- 171 R. Zhang, F. Liu and B. Wang, *Catal. Sci. Technol.*, 2016, **6**, 8036–8054.
- 172 M. Roiaz, E. Monachino, C. Dri, M. Greiner, A. Knop-Gericke, R. Schlogl, G. Comelli and E. Vesselli, *J. Am. Chem. Soc.*, 2016, **138**, 4146–4154.
- 173 C. Zhi, R. Zhang and B. Wang, *Mol. Catal.*, 2017, **438**, 1–14.
- 174 S. C. Lee, J. S. Kim, W. C. Shin, M. J. Choi and S. J. Choung, *J. Mol. Catal. A: Chem.*, 2009, **301**, 98–105.
- 175 C. Dai, S. Zhang, A. Zhang, C. Song and X. Guo, *J. Mater. Chem. A*, 2015, **3**, 16461–16468.
- 176 J. Kang, S. Zhang, Q. Zhang and Y. Wang, *Angew. Chem., Int. Ed.*, 2009, **48**, 2565–2568.

